Quasistatic anisotropic induced behaviour of a tatb-based plastic-bonded explosive

Gaëtane Plassart, Didier Picart, Michel Gratton, Arnaud Frachon, Michael Caliez

QUASISTATIC ANISOTROPIC INDUCED BEHAVIOUR OF A TATB-BASED PLASTIC-BONDED EXPLOSIVE

Gaëtane Plassart[1,2*], Didier Picart[1], Michel Gratton[2], Arnaud Frachon[2], Michaël Caliez[2]

[1] CEA DAM Le Ripault, F-37260 Monts, France
[2] INSA Centre Val de Loire, Univ. Orléans, Univ. Tours, LaMé, EA 7494, F-41000, Blois, France
[*] Corresponding author: gaetane.plassart@gmail.com

Abstract

The constitutive law of a plastic-bonded explosive (PBX) based on TATB crystals is studied in the quasistatic loading range. The experimental data highlight a viscoelastic behaviour with damage, and an anisotropy induced by plastic flow. The existing models for PBXs being not appropriate, a constitutive law accounting for the observed mechanisms is proposed. The linear viscoelasticity is integrated in a microplane model describing an effective anisotropic damage. A multilayer viscoplasticity is used to yield a non-linear kinematic hardening. A von Mises yield criterion is defined on each surface and a dilatancy function describes the volumetric plastic yield. This law is implemented in the Abaqus/Standard finite element code in the form of a UMAT subroutine. The model is calibrated on ten tests. The simulations performed to compare the model to each experimental test correctly reproduce the behaviour of the studied explosive composition.

Keywords

Plastic-bonded explosives. Constitutive law. Quasistatic mechanical behaviour. Load-induced anisotropy. Non-linear kinematic hardening. Anisotropic damage. Viscoelasticity. Viscoplasticity.

1. Introduction

When designing a pyrotechnic structure, simulations must be performed to assess mechanical strength. This step consists, in particular, in developing and implementing a constitutive law for the energetic material. In addition, the thermomechanical stresses that such a material undergoes during its life cycle can alter its microstructure. It can potentially modify its mechanical and/or reactive behaviour. To guarantee the safety and reliability of pyrotechnic structures, understanding and modelling the thermomechanical behaviour of these materials is essential. The CEA (Commissariat à l'Energie Atomique et aux Energies Alternatives – French Alternative Energies and Atomic Energy Commission) has developed several explosive compositions. In this paper, the plastic-bonded explosive (PBX) of interest is called M2. It is made of more than 95 wt% TATB crystals (1,3,5-triamino-2,4,6-trinitrobenzene), mixed with a polymeric binder. Other TATB-based PBXs frequently mentioned in the literature are PBX-9502 (95 wt% TATB, 5 wt% Kel-F 800 binder), LX-17-1 (92.5 wt% TATB, 5 wt% Kel-F 800 binder). In the literature, many studies have also been carried out on HMX (octahydro-1,3,5,7-tetranitro-1,3,5,5,7-tetrazocine)-based PBXs as PBX9501 (95 wt% HMX, 2.5 wt% estane, and 2.5 wt% nitro-plasticizer) or M1 (approximately 95 wt% of HMX mixed with a binder). Compaction of these TATB-or HMX-based compositions is obtained by hot isostatic compression (Picart, 1993; Thompson and Wright, 2004). The residual porosity is less than 5%. They are isotropic in their initial state.

Quasistatic constitutive laws have been developed for PBXs since the 1980s. A distinction is made between macroscopic and micromechanical models. The micromechanical models capture the mechanisms at the grain scale. They help understand the influence of the different components on the macroscopic response (Clements and Mas, 2004; Tan *et al.*, 2005, 2007; Wu and Huang, 2009; Ambos *et al.*, 2015; Arora *et al.*, 2015; Gasnier *et al.*, 2018; Trumel *et al.,* 2019). However, these models cannot be used in industrial context because of their prohibitive cost. The macroscopic quasistatic models proposed for PBXs have been compared by Plassart *et al.* (2020a). These models are:

- the SCRAM model (Statistical CRAcks Mechanics) (Dienes, 1978, 1996; Dienes *et al.*, 2006), an elasto-plastic model with anisotropic damage, for PBX-9501,
- the ViscoSCRAM model (Bennett *et al.*, 1998; Hackett and Bennett, 2000), an isotropic version of SCRAM adding a viscoelastic component, for PBX-9501,
- the model of Liu *et al.* (2019), a viscoplastic version of the ViscoSCRAM model, for PBX-9502,
- the model of Buechler (2012b, 2013), a viscoelastic-viscoplastic model with isotropic damage, for PBX-9501,
- the model of Zubelewicz *et al.* (2013), an elasto-viscoplastic model with anisotropic damage, for PBX-9502.

Unfortunately, the modelling choices were not based on experimental evidence. For example, the calibration of an anisotropic damage law was only done by observing the longitudinal response during compression tests, without measuring the transverse one. It explains the multitude of models without one of them emerging to describe the behaviour of this class of materials. Therefore, an in-depth characterization of the mechanical behaviour of M1 and M2 have been made. For the composition M1 (Picart and Brigolle, 2010; Le et al., 2010; Picart et al., 2014; Picart and Pompon, 2016), it yields a viscoelastic-plastic model with isotropic damage (Le, 2007, 2010; Caliez *et al.*, 2014) or an elasto-plastic model with anisotropic damage (Benelfellah, 2013; Benelfellah *et al.*, 2014, 2017; Picart *et al.*, 2014). These models have better reproduced the behaviour of M1 than the previous one. However, they poorly reproduce the hysteresis observed during loading/unloading cycles. The model proposed below for the M2 composition allows to understand the cause.

The experimental quasistatic behaviour of the TATB-based PBX M2 has been extensively characterised in Plassart *et al.* (2020a) and is summarized in section 2. The authors showed that HMX- and TATB-based PBXs have quite similar macroscopic properties: a quasi-brittle response with tensile/compressive asymmetry; strain rate-, temperature- and pressure dependencies; inelastic strains; a load-induced anisotropy. Therefore, a unique constitutive law is attainable for this class of materials in the quasistatic loading range. This is the aim of this paper. Each explosive composition would have its own set of parameters reinforcing the influence of particular deformation mechanisms.

For the explosive composition M2, the main deformation mechanism is the plasticity flow. In section 3, a viscoelastic-viscoplastic model, with effective load-induced anisotropic damage and a non-linear kinematic hardening, is developed and implemented. It is calibrated on M2. To the authors' point of view, the scientific novelty is based on the following key points. The first one is the strong link between the experimental study (described in Plassart *et al.*, 2020a) and the model proposed here. The phenomena have been isolated and studied in detail. Numerous simulations performed with various loading paths are compared to the corresponding data. The agreement between the simulations and this large database strongly validates the approach (see section 4). The second key point concerns unloadings. The study of loadings/unloadings has required to reject the popular Armstrong-Fredericks model. The older approach of Mroz allows reproducing correctly the hysteresis as well as monotonic tests. This suggests a good ability of the model to describe alternating loadings. In addition, it is uncommon in the literature to calibrate a kinematic strain hardening to model unloadings, without any isotropic strain hardening. The third key point concerns the consideration of pressure. The behaviour of explosive compositions, commonly pressure-dependent, often leads to a Drucker-Prager yield flow stress. However, despite the very high granular solid fraction of the M2 material, both the independence of the plasticity threshold to pressure and the plastic viscosity evolving with pressure have been experimentally demonstrated. Those choices are rarely found in the literature.

2. Characterization of the TATB-based material M2

2.1. Material

M2 is composed of about 95% by weight of TATB grains bonded by a thermoplastic binder. The mean diameter of TATB grains is about 50 µm. The material is obtained by coating the grains with a thin layer of polymeric binder. A granulation process leads to millimetric meta-grains. The granules are then subjected to several isostatic compression cycles at a temperature of about 150°C and a pressure cycle of 200 MPa (Picart, 1993). After cooling, a coherent material is obtained, and samples can be manufactured. Due to the compaction process, the residual porosity is only a few percent. **Figure 1** shows a micrograph of the material

M2. The colour variations are due to a strong anisotropy of the TATB grains on the microscale. However, as the orientation of the grains and the binder are randomly distributed, the material is initially isotropic on a macroscale. All the tests described in this paper were performed on the same batch.

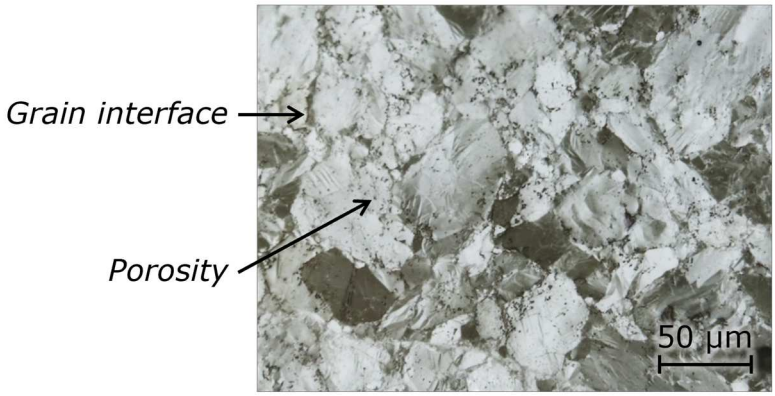

Figure 1. *Micrograph of material M2. The color variations are due to the anisotropy of the TATB grains. Porosity is mainly located inside the grains (small black dots) and at the grain/grain interfaces.*

2.2. Experimental observations, guidelines for model

A complete experimental characterization of M2 has been presented by Plassart *et al.* (2020a). In the following, the key features of the behaviour are summarised. We refer the reader to the original paper for details on test procedures and their repeatability. All the mechanical tests performed on the material M2 are listed in **table 1**. The corresponding curves (stress-strain or waveforms) are in the article and the supplementary materials of Plassart *et al.* (2020a).

In this paper, the influence of temperature is not considered. The analysis of the behaviour is limited to a temperature of 20°C. For details on the temperature influence, see Plassart *et al.* (2020a) and Plassart (2020b).

Uniaxial compression	Longitudinal / transversal strains Temperature Strain rate Creep / relaxation Load – unload cycles	✓ / ✓ -30°C à 80°C 10^{-6} s^{-1} à 10^{-4} s^{-1} ✓ ✓
Uniaxial tensile	Longitudinal / transversal strains Temperature Strain rate Creep / relaxation Load – unload cycles	✓ / ✓ -30°C à 80°C 10^{-6} s^{-1} à 10^{-4} s^{-1} ✓ ✓
Torsion	Shear strains Temperature Strain rate Creep / relaxation Load – unload cycles	✓ 20°C $0.01°.s^{-1}$ ✗ ✓
Triaxial compression	Longitudinal / transversal strains Pressure Temperature Strain rate Creep / relaxation Load – unload cycles	✓ / ✓ 2.5, 5 and 10 MPa 20°C 10^{-5} s^{-1} ✓ ✓
Alternating loading	Longitudinal / transversal strains Temperature Strain rate Creep / relaxation Load – unload cycles	✓ / ✓ 20°C 10^{-5} s^{-1} ✓ ✓
Other tests	DMA	0°C to +90°C
	Multiaxial tests	Brazilian test, channel-die, equibiaxial compression, three-point bending

Table 1. *Mechanical tests performed on the material M2 (from Plassart et al., 2020a).*

Among the key points of the behaviour, an asymmetry between the tensile and compression responses is observed. This is common for quasi-brittle granular materials (see Mazars *et al.*, 1990 for concrete; Thomson *et al.*, 2010 for PBX-9502; Buechler, 2012a for PBX-9501; and Picart *et al.*, 2014 for M1). There is no clear transition to plasticity. The Young's modulus is independent of the stress sign (compression or tensile), the strain rate and the pressure from 0 to 10 MPa. These observations differ from that made on HMX-based PBXs (Wiegand *et al.*, 2011; Picart *et al.*, 2014). The ratio of the transversal to the longitudinal strain (Poisson's ratio at low strain) is independent of the strain rate and the stress sign, but there is a non-linear effect of pressure. It decreases below 5 MPa and then increases. In addition, dynamic mechanical analysis (DMA) tests highlighted the linear viscoelastic behaviour of M2 at low stress levels (1 MPa).

Cyclic compression and tensile tests were also performed on M2. **Figure 2** shows an example of cyclic compression. Each cycles had four phases: (1) a strain rate controlled load, (2) a stress relaxation at fixed longitudinal strain, (3) a strain rate controlled unload, (4) a strain recovery at rest. These tests are inspired by those performed on M1 (Gratton *et al.*, 2009; Le *et al.*, 2010). The relaxation and recovery steps enable removing the viscous trends of M2. The amount of the stress that relaxes during the dwell is denoted as the "relaxed stress". The strains at the end of the recovery step highlight the irreversible strains suffered by the material. As for M1 (Le *et al.*, 2010), the comparison between cyclic and monotonic curves shows that the cyclic test envelope corresponds to the monotonic test one. Adding cycles does not influence the envelope behaviour of M2.

Moreover, the transversal strain grows faster than the longitudinal one. So, M2 develops a load-induced anisotropy. The latter could be due to damage. The evolution of the elastic modules during loading/unloading has been studied. An elastic stress state is assumed at the beginning of each load and unload. Tangent modules are calculated in load (**figure 2**, in blue) and unload (**figure 2**, in red). They are determined by linear regression over a strain window of 0.05%. All modules being similar, no damage is visible. Moreover, the influence of the stress level on the elastic modules is negligible. So, the assumption of a linear viscoelasticity is possible.

Figure 3 shows the evolution of longitudinal (left), and transversal (right) modules measured under cyclic loading in uniaxial compression (black lines), triaxial compression at 10 MPa pressure (blue line) and uniaxial tensile (red lines) at 20°C. The three rates applied in uniaxial loading are distinguished (lines, dotted and dashed lines). For each condition, the test leading to the maximum modulus degradation is shown. In uniaxial compression, a decrease about 500 MPa (respectively 5000 MPa) is observed for the longitudinal (resp. transversal) modulus. These degradations are independent of the strain rate because line and dotted curves show a similar decrease. Using the samples tested at 20°C (independently of the strain rate), the 95% confidence interval of the initial longitudinal modulus is 900 MPa. It is 3000 MPa for the transversal modulus. Since the decrease in longitudinal modulus is within its confidence interval, no significative longitudinal damage is observed. Conversely, since the decrease of the transversal modulus is larger than its confidence interval. Therefore, a slight transversal damage is developing (less than 20% at failure). This results in zero volumetric damage and a maximum deviatoric damage of 12%. About the triaxial test, the modules evolution is not linear. The slope of the last four transversal modules is the same as in uniaxial compression. Therefore, damage is pressure-independent. The tensile tests did not reveal any considerable damage. They fail at a strain corresponding to the beginning of the modules degradation in compression. The damage of the TATB-based PBX M2 at 20°C thus develops late. Its influence on the global behaviour of the material is limited.

Damage evolution is usually estimated assuming an elastic unloading (see for concrete, Benouniche, 1979; Gotuwka, 1999) and for HMX-based PBXs (Gratton *et al.*, 2009; Le *et al.*, 2010; Picart *et al.*, 2014). For each cycle, the secant modulus between the end of the relaxation and the end of the recovery is presumed elastic (**Figure** , in green). The secant modules measured on M2 strongly decreases during the loading when the tangent modules remain unchanged. The variations of the secant modules cannot be due to damage. The evolution of the secant modules could be due to plasticity. This interpretation is discussed below.

An experimental campaign of alternating tensile/compression was also performed on M2. Two kinds of tests were conducted: (1) a compression up to ~0.95 σ_{max} (σ_{max} is the peak stress in compression) followed by a tensile loading to failure, and (2) a traction up to ~0.95 σ_{max} (σ_{max} is the peak stress in tensile test) followed by a compression loading to failure. When quasi-brittle granular materials are submitted to alternating tensile/compression, a stiffness recovery is commonly observed at the beginning of compression (Mazars *et al.*, 1990; Picart *et al.*, 2014). This phenomenon is called unilateral effect and is related to damage by microcracking. For M2, no recovery of stiffness is observed. This is consistent with the negligible damage of the material.

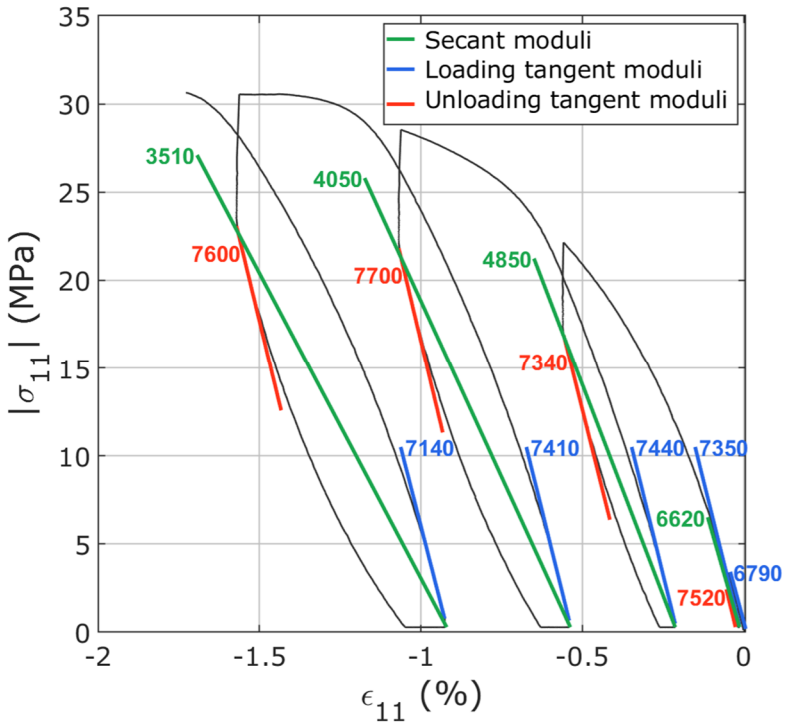

Figure 2. *Secant and tangent longitudinal modules for a cyclic compression test (from Plassart et al., 2020a). Secant modules decrease can not be interpreted as a damage effect since the tangent modules do not show any evolution.*

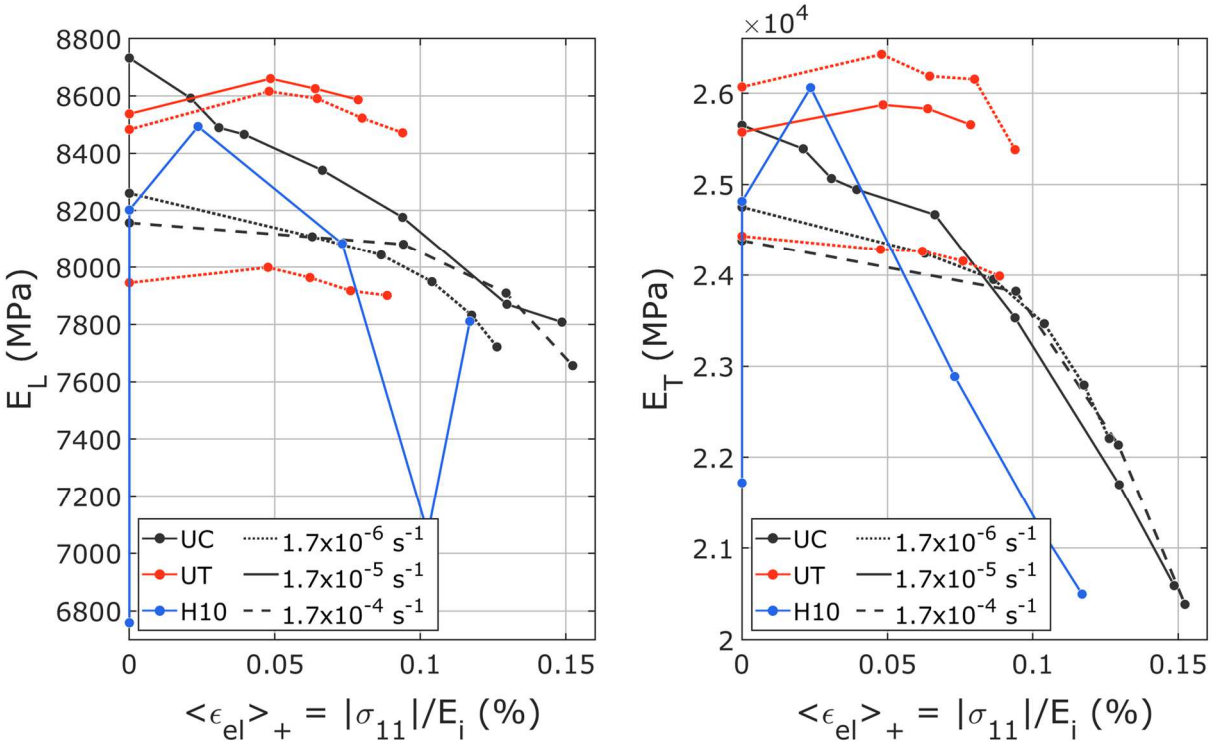

Figure 3. *Evolution of elastic modules in uniaxial compression (« UC »), uniaxial tensile test (« UT ») and triaxial compression at 10 MPa pressure (« H10 ») at 20°C as a function of the positive elastic strains at three strain rates. The positive strains are calculated from the elastic transversal modulus (i=T) in compression, and elastic longitudinal modulus in tensile loading (i=L).*

A linear viscoelastic model based on the DMA data has been developed. It cannot by itself reproduce the non-linear response of the material up to failure nor the whole relaxation of the stress (respectively recovery

of the strain) when the longitudinal strain (resp. the stress) is constant. During relaxation, only 20% of the stress evolution can be obtained using the linear viscoelastic model based on DMA data. Therefore, a plastic strain mechanism is added in series with the viscoelastic model.

The analysis of the uniaxial compression, triaxial compression, uniaxial tensile and torsion curves shows that the behaviour is non-linear starting from about 4 MPa of equivalent von Mises stress, whatever the strain rate. These observations show that the initial yield surface of M2 is pressure- and strain-independent. It could be represented by a von Mises criterion.

The experimental campaign providing the most information on M2 is an alternating compression test. Two compressions at 30 MPa were performed successively to highlight the load-induced anisotropy of M2, the latter being observed during a second loading in a different direction (Cambou and Lanier, 1988; Lanier *et al.*, 1991). The curves are compared in **figure 4**. The first compression is in red, the 0° reloading is in blue, the 90° reloading is in green and all the inversed unloadings are in grey (see Plassart *et al.*, 2020 for details). The blue and green curves are clearly different. The green curve shows more strain than the red one. Lastly, the maximum strain for the blue curve is half that of the green curve. So, the 90° direction (in green), stretched during the first loading, is more ductile than initially. Conversely, the 0° direction (in blue), compressed during the first loading, is more rigid above a stress of 15 MPa. The anisotropy induced by the first load is obvious. This induced anisotropy cannot be attributed to a negligible damage, as previously demonstrated. This observation is confirmed by the fact that the elastic modules (the initial slope of the curves) are not influenced by the first load. Furthermore, the unloading curves (in grey) match with the 0° reloading one (in blue). Also, the 0° reloading and the initial loading (in red) are overlapped up to 15 MPa. The behaviour revealed by these observations can be interpreted using a kinematic hardening plasticity model (Plassart *et al.*, 2020a). An isotropic strain hardening would fail to reproduce these phenomena.

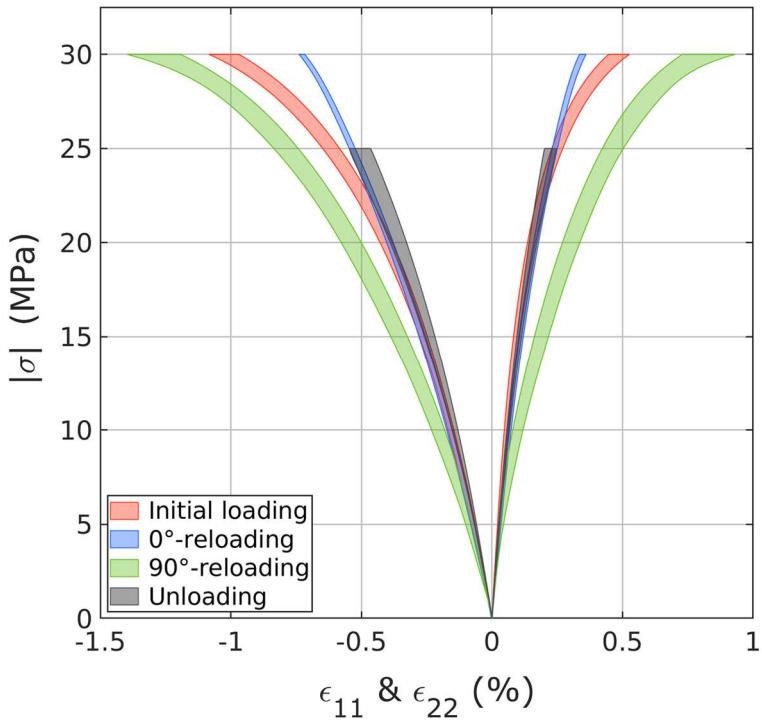

***Figure 4**. Comparison of the loading and unloading curves of the 0°-0° and 0°-90° tests (from Plassart et al., 2020a). The response depends on the reloading direction highlighting a load-induced anisotropy during the first loading.*

The kinematic hardening should be non-linear to reproduce the strong non-linearity observed in compression. A popular non-linear kinematic hardening is the Armstrong-Frederick model (Armstrong and Frederick 1966, 2007). A cumulative plasticity term is added to the linear Prager strain hardening. Therefore, the strain hardening modulus is related to the accumulated plastic strain. The total strain at a given stress is dependent on the number of cycles previously performed. Consequently, a monotonic curve is necessarily

different from the envelope curve of a cyclic test. This is not the case for the M2 composition. Cyclic and monotonic tests have the same envelope behaviour. The Armstrong-Frederick model also leads to stiffer unloading than reloading, which is not observed during experiments on M2. Chaboche et al. (1979) proposed a model based on "parallel" mechanisms in the sense of stress (and hardening) additivity. The non-linearity is due to an evanescent strain memory which is a cumulative plasticity. Therefore, for the same reasons as the Armstrong-Frederick model, this model does not meet our expectations.

A multilayer model (Mroz, 1967) is preferred to reproduce the experimental observations. Several linear Prager hardening modules are added in series. So, there is a strain additivity. It is equivalent to nest several yield surfaces. The global hardening modulus is non-linear because each surface has a different kinematic modulus and yield strength. The activation of a new surface decreases the global hardening modulus. This model can be qualified as "multilinear". It is schematically described in **figure 5**.

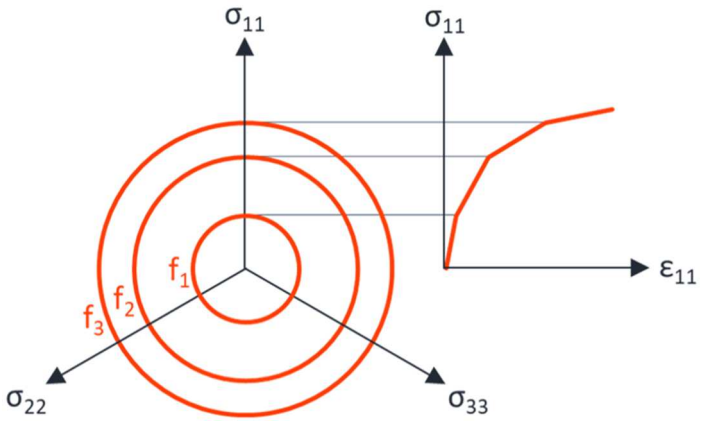

Figure 5. *Scheme of the multilayer model of Mroz (Mroz 1967) with three yield surfaces. f_i are the yield criterion of each surface. When a surface is reached, it moves to the next one, then the two move together. The global hardening modulus decreases when a surface is activated.*

A repeated torsional cycling test, no presented in Plassart *et al.* 2020a was performed on M2. The angular rate was controlled up to a torque corresponding to a stress of ±6 MPa on the average radius of the sample. The test was stopped after twenty cycles without reaching failure. It was carried out with the same procedure as the monotonic torsion tests (Plassart *et al.*, 2020a). The second and twentieth cycles are identical. **Figure 6** shows that the material has an immediate accommodation in cyclic test at zero mean stress. Since there is no cyclic softening nor strain hardening in alternating torsion, adding isotropic strain hardening is inappropriate. It would increase the apparent yield strength over several cycles due to viscoplastic flow.

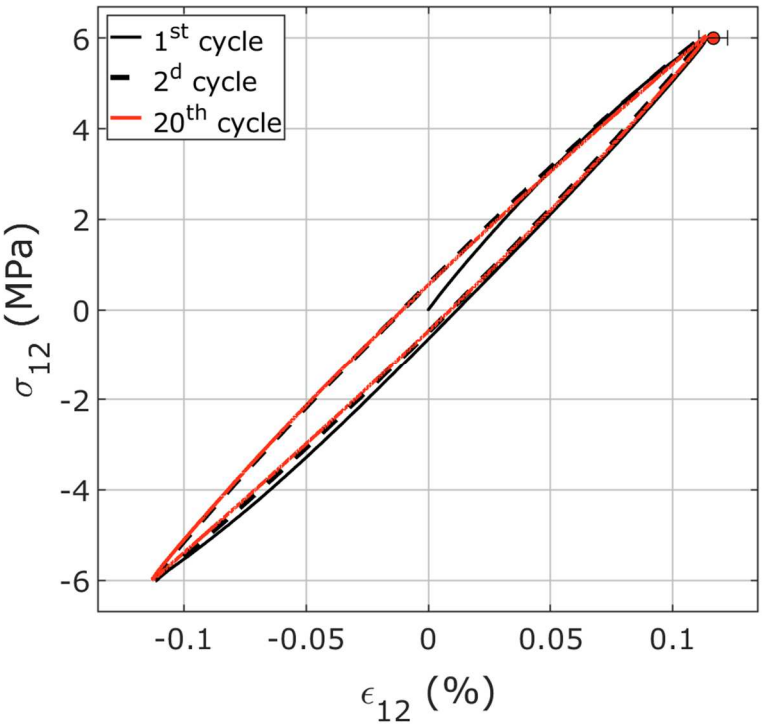

Figure 6. *Alternating torsion test performed at 0.015°.s^{-1} and cycled twenty times.*

Another point to focus is the pressure-dependence. The yield criterion and the elastic modules are pressure independent. The same is assumed for the viscoelastic characteristic times. Two constitutive laws are then possible: integrating the pressure effect on the kinematic hardening or on the viscoplastic flow. Rinaldi (2006) and Dasriaux (2013) showing that pressure slows down the plastic flow of polymers, the latter is adopted.

Lastly, during a compression test a strong non-linearity of the volumetric behaviour is observed, with a transition from contraction to dilatation (Plassart *et al.*, 2020a). A similar observation was made for many granular materials (Green and Swanson, 1973; Van Mier, 1894, 1986; Homand-Etienne *et al.*, 1998; Hu, 2010). Therefore, viscoplastic flow and kinematic hardening must address the volumetric component of the behaviour. With a von Mises criterion, a non-associated flow rule is needed. The determination of a flow potential being thermodynamically complicated, an indirect method is followed: the volumetric part is related to the deviatoric one by a dilatancy function.

To conclude, the explosive composition called M2 shows strain rate-, temperature- and pressure-dependence, inelastic strain, and a load-induced anisotropy. The strain additivity is justified, as is the use of a linear viscoelastic component. Damage being not the main deformation mechanism for the composition M2, the non-associated viscoplastic flow governs the material “ductility”. The load-induced anisotropy can be reproduced using a non-linear kinematic strain hardening. Isotropic strain hardening must be avoided.

The temperature dependence is out of the scope of this paper. The modelling only focuses on the strain rate and pressure dependencies at 20°C. For information on the integration of the temperature dependence, the reader will see Plassart 2020b.

3. Modelling

The relevance of the models from the literature for HMX- and TATB-based PBXs is questionable due to their insufficient experimental justification (Plassart *et al.* 2020a). For this class of materials, only M1 (an HMX-based PBX) and M2 (a TATB-based PBX) have been deeply characterized to highlight deformation mechanisms (Picart *et al.*, 2014; Plassart *et al.* 2020a). The main difference is their level of damage (Benelfellah, 2013; Picart *et al.*, 2014). M2 develops a load-induced anisotropy attributed to plastic flow when the load-induced anisotropy of M1 is due to damage. For the latter, the transversal to the longitudinal strains

ratio can exceed 0.5 and a unilateral effect was observed. In addition, its Young's modulus is pressure-dependent. Despite these differences, the two explosive compositions M1 and M2 have quite similar macroscopic properties. It gives confidence on the rise of a single constitutive law for this class of materials.

Giving the discussion on section 2 and the model proposed by Benelfellah *et al.* (Benelfellah, 2013; Picart *et al.*, 2014) for M1, the constitutive law must incorporate a viscoelastic part in series with a viscoplastic one. A load-induced anisotropy by damage and a non-linear kinematic strain hardening mechanisms must be incorporate. The single law proposed for this class of materials is detailed in the next paragraphs.

3.1. Formulation

A new macroscopic constitutive law is now proposed and calibrated on the TATB-based PBX M2. The proposed model is written in the framework of generalized standard materials. The formalism is that of Lemaître *et al.* (2020). The specific Helmholtz free energy ψ is chosen as the state potential. It is a function of the observable variable $\underline{\underline{\varepsilon}}$ and the internal variables defining the material history (**table 2**). The viscoelastic and viscoplastic components are in series. Assuming they are uncoupled, the state potential can be decomposed in a viscoelastic potential ψ_{ve} and a viscoplastic one ψ_{vp} (Lemaître *et al.*, 2020). The viscoelastic potential is split in volumetric ${\psi_{ve}}^{V}$ and deviatoric ${\psi_{ve}}^{D}$ parts. The decomposition of the free energy and its expression are summarized in **figure 8**. A rheological scheme of the behaviour law is given **figure 9**.

3.1.1. Viscoelastic part

The viscoelastic behaviour is described by a generalized Maxwell model (both on the volumetric and deviatoric components). Following the work of Benelfellah *et al.* (Benelfellah, 2013; Picart *et al.*, 2014), a microplane model is introduced on the viscoelastic part. In this discrete model, each fixed direction of the solid angle is characterized by a plane of normal $\underline{n}$. The strain tensor is projected on each microplane, which enables working with scalar and vector quantities. Here, a volumetric-deviatoric (VD) formulation is chosen (Leukart and Ramm, 2002, 2003). Kinematic constraints define volumetric ${\varepsilon_{ve}}^{V}$ and deviatoric $\underline{{\varepsilon_{ve}}^{D\,mic}}$ strains as the projections on the microplane of the viscoelastic strain tensor $\underline{\underline{\varepsilon_{ve}}}$ (Carol *et al.*, 2001):

$$\begin{cases} {\varepsilon_{ve}}^{V} = \underline{\underline{V}} : \underline{\underline{\varepsilon_{ve}}} \\ \underline{{\varepsilon_{ve}}^{D\,mic}} = \underline{\underline{\underline{\underline{D}}}}^{mic} : \underline{\underline{\varepsilon_{ve}}} \end{cases} \quad \text{with:} \quad \begin{cases} \underline{\underline{V}} = \dfrac{1}{3}\,\underline{\underline{1}} \\ \underline{\underline{\underline{\underline{D}}}}^{mic} = \underline{n}.\underline{\underline{\underline{\underline{I}}}}^{D} \end{cases} \tag{1}$$

$\underline{\underline{V}}$ and $\underline{\underline{\underline{\underline{D}}}}^{mic}$ are the projection tensors. $\underline{\underline{1}}$ is the second order identity tensor. $\underline{\underline{\underline{\underline{I}}}}^{D}$ is the deviatoric part of the fourth order identity tensor. The deviatoric component is decomposed on the different microplanes while the volumetric one is not. The exponent *mic* indicates the dependence on the microplane of normal $\underline{n}$.

Two equivalent methods are possible to couple the Maxwell viscoelastic model to the microplane damage model (Chatti *et al.*, 2019): (1) in the external approach, the microplane model is put in series with the Maxwell one; (2) in the internal approach, the Maxwell model is integrated within the microplanes. The latter, easier to implement, is chosen. The calculations are therefore reduced to scalar equations, while the external approach involves fourth order tensors to invert.

The fundamental assumption ensuring the thermodynamic stability of microplane models has been postulated by (Carol et al., 2001). It states that the total free energy corresponds to the integral over the solid angle of the energies defined on each microplane. After discretization of the solid angle, the deviatoric viscoelastic free energy ${\psi_{ve}}^{D}$ is the sum of the viscoelastic deviatoric free energies of each microplane ${\psi_{ve}}^{D\,mic}$. An angular weighting coefficient ω^{mic} related to the number N_m of microplanes gives a balance to microplanes (Bažant and Oh, 1985) (**figure 8**, *projection on microplanes*).

The generalized Maxwell model involves a purely elastic branch (index ∞) and N_b viscoelastic ones featuring an elastic stiffness (index *elast*) and a viscous dashpot (index *visc*). The bulk and shear modules of the b^{th} viscoelastic branch are respectively noted k_{Vb} and μ_{Db} ($k_{V\infty}$ and $\mu_{D\infty}$ for the elastic branch). The volumetric $\psi_{ve}{}^{V}$ and the deviatoric free energies of the microplane $\psi_{ve}{}^{D\,mic}$ are the sum of the free energies of each branch. A damage term d_V (respectively $d_D{}^{mic}$) affects the elastic modulus k_{Vb} and $k_{V\infty}$ (respectively μ_{Db} and $\mu_{D\infty}$). A function α_{Vb} weights the volumetric damage effectivity on each viscoelastic branch ($\alpha_{V\infty}$ for the elastic branch). The postulated expression of the free energy of each branch is given **figure 8**.

The damage variables d_V and $d_D{}^{mic}$ are respectively related to the volumetric and the deviatoric strain of the purely elastic branch from potentials noted $Y_{V\infty}$ and $Y_{D\infty}{}^{mic}$:

$$Y_{V\infty} = \frac{1}{2}\, k_{V\infty}\, \varepsilon_{ve}{}^{V\,2} \quad ; \quad Y_{D\infty}{}^{mic} = \frac{1}{2}\, \mu_{D\infty}\, \underline{\varepsilon_{ve}{}^{D\,mic}} . \underline{\varepsilon_{ve}{}^{D\,mic}} \tag{2}$$

so, they are independent of the branch. They range between 0 and 1 and cannot decrease. Their evolution law is determined from the experimental degradation of the bulk and shear modules.

The definition of the damage effectivities must meet the thermodynamic consistency. The stress-strain response must be continuous. Benelfellah *et al.* (Benelfellah, 2013; Picart *et al.*, 2014) have chosen the simplest formulation. Effectivity is defined as Heaviside function of its corresponding elastic strain. In VD formulation, the deviatoric component is vectorial. Only the volumetric component enables the definition of such a function. The α_{Vb} effectivity is related to the strain $\varepsilon_{ve}{}^{V}{}_{b,elast}$. For the purely elastic branch, $\alpha_{V\infty}$ is related to $\varepsilon_{ve}{}^{V}$.

The sum of the stresses of each branch defines a hydrostatic pressure σ^V independent of the microplane and a deviatoric stress on each microplane $\underline{\sigma^{D\,mic}}$:

$$\begin{cases} \sigma^V = \sigma^V{}_\infty + \sum_{b=1}^{N_b} \sigma^V{}_b \\ \underline{\sigma^{D\,mic}} = \underline{\sigma^D{}_\infty}{}^{mic} + \sum_{b=1}^{N_b} \underline{\sigma^D{}_b}{}^{mic} \end{cases} \tag{3}$$

The stresses $\sigma^V{}_\infty$ and $\underline{\sigma^D{}_\infty}{}^{mic}$ are the hydrostatic pressure and the deviatoric stress of the purely elastic branch. The stresses $\sigma^V{}_b$ and $\underline{\sigma^D{}_b}{}^{mic}$ are the hydrostatic pressure and the deviatoric stress of the b^{th} viscoelastic branch.

The behaviour of the elastic branch is linear when damage is constant:

$$\begin{cases} \sigma^V{}_\infty = (1\text{-}\alpha_{V\infty} d_V)\, k_{V\infty}\, \varepsilon_{ve}{}^{V} \\ \underline{\sigma^D{}_\infty}{}^{mic} = \left(1\text{-}d_D{}^{mic}\right) \mu_{D\infty}\, \underline{\varepsilon_{ve}{}^{D\,mic}} \end{cases} \tag{4}$$

The volumetric and deviatoric differential equations ruling the behaviour of each viscoelastic branch are:

$$\begin{cases} \dot{\sigma}^V{}_b + \left(\frac{1}{\tau_b} + \frac{\alpha_{Vb}\,\dot{d}_V}{1\text{-}\alpha_{Vb} d_V}\right) \sigma^V{}_b = (1\text{-}\alpha_{Vb} d_V)\, k_{Vb}\, \dot{\varepsilon}_{ve}{}^{V} \\ \underline{\dot{\sigma}^D{}_b}{}^{mic} + \left(\frac{1}{\tau_b} + \frac{\dot{d}_D{}^{mic}}{1\text{-}d_D{}^{mic}}\right) \underline{\sigma^D{}_b}{}^{mic} = \left(1\text{-}d_D{}^{mic}\right) \mu_{Db}\, \underline{\dot{\varepsilon}_{ve}{}^{D\,mic}} \end{cases} \tag{5}$$

the dot above a variable means that it is its time derivative. The principle of virtual work enables deducing the total stress $\underline{\underline{\sigma}}$ (Carol *et al.*, 2001):

$$\underline{\underline{\sigma}} = \sigma_V \underline{\underline{V}} + \sum_{mic=1}^{N_m} 3\,\omega^{mic}\,\underline{\sigma_D}^{mic}.\underline{\underline{\underline{\underline{D}}}}^{mic} = \sigma_V \underline{\underline{V}} + \sum_{mic=1}^{N_m} 3\,\omega^{mic}\,\underline{\underline{\underline{\underline{D}}}}^{mic^T}.\underline{\sigma_D}^{mic} \tag{6}$$

with $\underline{\underline{\underline{\underline{D}}}}^{mic^T}$ the transposed tensor of $\underline{\underline{\underline{\underline{D}}}}^{mic}$. As the viscoelasticity and viscoplasticity are added in series, the stress tensor $\underline{\underline{\sigma}}$ also applies to the viscoplastic part.

3.1.2. Viscoplastic part

A number N_s of yield surfaces are put in series in the sense of the plastic strain additivity to define a non-linear viscoplastic strain $\underline{\underline{\varepsilon_{vp}}}$. s is the index of the surface number. The viscoplastic free energy ψ_{vp} is therefore the sum of the free energies of each surface $\underline{\underline{\psi_{vp\,s}}}$. The latter depend only on the kinematic hardening variable $\underline{\underline{\xi_s}}$, homogeneous to a strain. Free energies are chosen to follow the linear strain hardening law of Prager (**figure 8**). The hardening modulus of the surface s is denoted C_s.

A surface s is defined by its yield stress σ_{Y_s} and its kinematic hardening tensor $\underline{\underline{X_s}}$. The von Mises yield criterion f_s is written in the effective stress space:

$$f_s = \left|\underline{\underline{\tilde{\sigma}}}^D - \underline{\underline{X_s}}\right| - \sigma_{Y_s} \tag{7}$$

The effective stress $\underline{\underline{\tilde{\sigma}}}$ is related to the stress $\underline{\underline{\sigma}}$ by an effectivity tensor $\underline{\underline{\underline{\underline{M}}}}$ depending on the state of damage:

$$\underline{\underline{\tilde{\sigma}}} = \underline{\underline{\underline{\underline{M}}}}^{-1} : \underline{\underline{\sigma}} \;\Rightarrow\; \begin{cases} \sigma^V = M^V \tilde{\sigma}^V \\ \underline{\underline{\sigma}}^D = \underline{\underline{\underline{\underline{M}}}}^D : \underline{\underline{\tilde{\sigma}}}^D \end{cases} \tag{8}$$

where $\tilde{\sigma}^V$ is the effective hydrostatic pressure and $\underline{\underline{\tilde{\sigma}}}^D$ is the effective deviatoric stress tensor. M^V and $\underline{\underline{\underline{\underline{M}}}}^D$ are the volumetric and deviatoric parts of $\underline{\underline{\underline{\underline{M}}}}$. The nature of the tensor $\underline{\underline{\underline{\underline{M}}}}$ is discussed below.

Without unilateral effect of damage, working in the effective stress space preserves the convexity of the yield surfaces. With a unilateral effect, a yield surface defined in effective stress is not convex and the yield criterion must be adapted (Liénard, 1989; Desmorat and Cantournet, 2008). Here, the effectiveness is carried by the volumetric component while the yield surfaces are only deviatoric. The convexity of the load surfaces is therefore preserved in effective stress space.

The plastic flow of the surfaces is not associated. The volumetric flow $\dot{\varepsilon}_{vp\,s}{}^V$ is related to the deviatoric one $\underline{\underline{\dot{\varepsilon}_{vp\,s}}}^D$ by the dilatancy function β. The deviatoric flow is normal to the load surface:

$$\begin{cases} \dot{\varepsilon}_{vp\,s}{}^V = \beta \left|\underline{\underline{\dot{\varepsilon}_{vp\,s}}}^D\right| \\ \underline{\underline{\dot{\varepsilon}_{vp\,s}}}^D = \dot{\lambda}_s \dfrac{\partial f_s}{\partial \underline{\underline{\sigma}}^D} = \dfrac{3}{2}\dot{\lambda}_s \dfrac{\underline{\underline{\tilde{\sigma}}}^D - \underline{\underline{X_s}}}{\left|\underline{\underline{\tilde{\sigma}}}^D - \underline{\underline{X_s}}\right|} : \underline{\underline{\underline{\underline{M}}}}^{D^{-1}} \end{cases} \tag{9}$$

In multilayer models (Mroz, 1967; Montáns, 2000, 2001; Yan and Oskay, 2017) the sliding direction of the surfaces is constrained such that they remain nested within each other (**figure 7 right**). They cannot overlap. The smallest surface moves first, until it becomes tangent to the second. The second surface becomes active from the contact. The two surfaces then remain tangent while moving. This pattern is repeated until

the last surface is reached. The last surface defines an associated flow. To our knowledge, no thermodynamic justification is given to this last constraint.

With viscoplastic flow, a surface could be activated when the previous one has not yet reached it. The classic Mroz surface displacement scheme is not applicable here. The sliding direction of a surface is along its normal and it is not constrained by other surfaces. So, surfaces can slightly overlap in non-proportional loadings (**figure 7 left**). This could be improved in future work. However, the simulations (presented below later in this paper) show a negligible overlap.

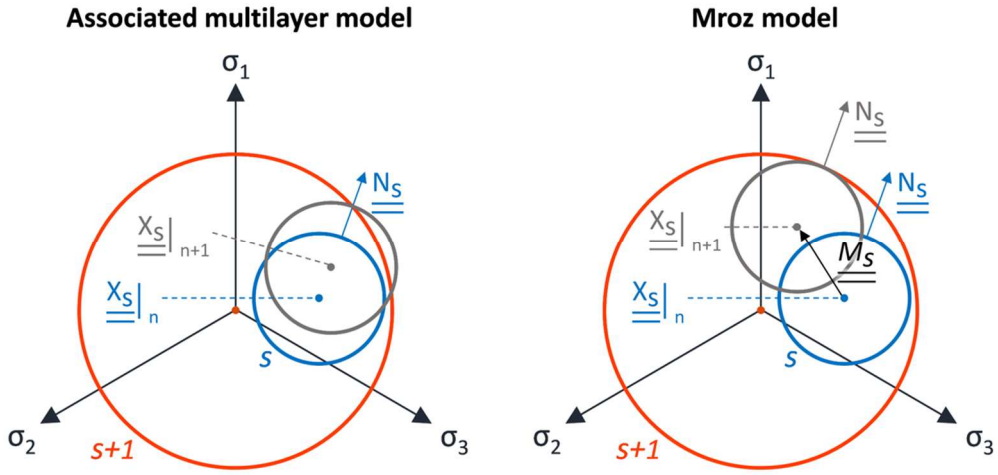

Figure 7. *Left, diagram representing the possible exit of surface s with respect to surface s+1 during non-proportional loading (negligible in the simulations below). Right, the solution provided by Mroz (1967) to ensure the nesting of the surfaces. The tensor* $\underline{\underline{N_s}}$ *is the flow direction. The tensor* $\underline{\underline{M_s}}$ *is the sliding direction of the surface* s.

Dilatancy is a function of the effective pressure $\tilde{\sigma}^V$ and the norm of the total deviatoric viscoplastic strain $\left|\underline{\underline{\varepsilon_{vp}}}^D\right|$. Its expression is determined from the experimental data. We work here with the norm of the viscoplastic strain $\underline{\underline{\varepsilon_{vp}}}^D$. It is an instantaneous measurement. Using the cumulative plasticity as Chiarelli (2000) and Le *et al.* (2010) is not suitable here. Numerically, given the kinematic strain hardening, there is an accumulation of the viscoplastic strain when unloading and reloading. At a same stress level, the accumulated viscoplastic strain depends on the number of cycles performed. To match our curve of a monotonic simulation with the envelope of the corresponding cyclic simulation, the instantaneous viscoplastic strain must be considered in the expression of the dilatancy.

The model being viscoplastic, the criterion outputs (f_s>0) are allowed. As seen in section 2, the pressure slows down the plastic flow of polymers (Rinaldi, 2006 ; Dasriaux, 2013). The viscoplastic multiplier $\dot{\lambda}_s$ of each surface follows a classical exponential-power law (Lemaître *et al.*, 2020), but with dependence on effective pressure $\tilde{\sigma}^V$:

$$\dot{\lambda}_s = \left(\frac{f_s}{a_1}\right)^n \exp\left(\left(a_2+a_3\tilde{\sigma}^V\right) f_s{}^{n+1}\right) \tag{10}$$

The pressure is effective as for the whole viscoplastic model. The coefficients a_1, a_2, a_3 and n are material parameters (same set for each surface). The a_3 parameter being positive, the greater the confinement, the slower the flow. The Norton term (power function) is dominant for low values of f_s while the exponential one dominates for higher values of f_s.

Each surface has a linear kinematic hardening defined by the Prager's law (**figure 8**). The thermodynamic force associated with $\underline{\underline{\xi_s}}$ is the kinematic hardening tensor $\underline{\underline{X_s}}$, homogeneous to a stress:

$$\underline{\underline{X_s}} = \frac{2}{3} C_s \underline{\underline{\xi_s}} \tag{11}$$

Note that the norm $\left|\underline{\underline{\tilde{\sigma}}}^D - \underline{\underline{X_s}}\right|$ in equation 7 corresponds to the second deviatoric invariant J_2 of the tensor $\left(\underline{\underline{\tilde{\sigma}}}^D - \underline{\underline{X_s}}\right)$.

The Prager's linear hardening law is written:

$$\underline{\underline{\dot{\xi}_s}} = -\dot{\lambda}_s \frac{\partial f_s}{\partial \underline{\underline{X_s}}} = \underline{\underline{\dot{\varepsilon}_{vp\,s}}}^D : \underline{\underline{\underline{\underline{M}}}}^D \tag{12}$$

hence:

$$\underline{\underline{\dot{X}_s}} = C_s \dot{\lambda}_s \frac{\underline{\underline{\tilde{\sigma}}}^D - \underline{\underline{X_s}}}{\left|\underline{\underline{\tilde{\sigma}}}^D - \underline{\underline{X_s}}\right|} \tag{13}$$

Finally, for the implementation of the law, the effectiveness tensor $\underline{\underline{\underline{\underline{M}}}}$ would only appear through the tensor $\underline{\underline{\underline{\underline{M}}}}^{D^{-1}}$ in the expression of $\underline{\underline{\dot{\varepsilon}_{vp\,s}}}^D$ (equation 9). To simplify the implementation of the deviatoric flow $\underline{\underline{\dot{\varepsilon}_{vp\,s}}}^D$, $\underline{\underline{\underline{\underline{M}}}}^{D^{-1}}$ is unity in this equation. This approximation is acceptable due to the low level of damage of the material M2. This simplification will have to be reconsidered when identifying the model to the material M1 which suffers more damage. For this material, the tensor $\underline{\underline{\underline{\underline{M}}}}$ will probably have to be calculated.

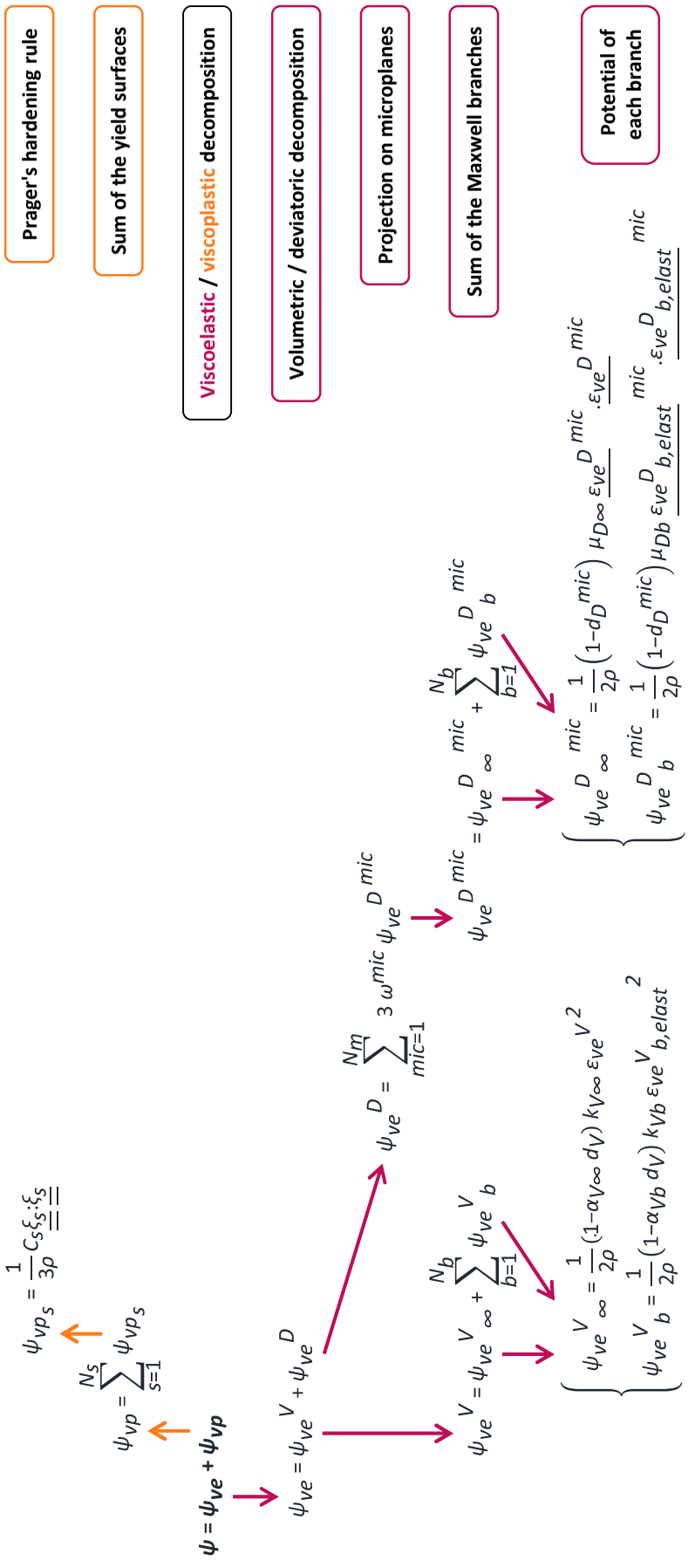

Figure 8. *Decomposition of the free energy. The variable ρ is the density of the material.*

Mechanisms	**Observable and internal state variables**	**Associated variables**	**Definition level** (state var. / associated var.)
	$\underline{\underline{\varepsilon}}$	$\underline{\underline{\sigma}}$	Global
Viscoelasticity	$\varepsilon_{ve}{}^{V}$	$\sigma^{V}{}_{b}$	global / branch
	$\underline{\varepsilon_{ve}{}^{D}}^{mic}$	$\underline{\sigma^{D}{}_{b}}^{mic}$	microplane / microplane branch
	$\varepsilon_{ve}{}^{V}{}_{b,elast}$	$\sigma^{V}{}_{b,elast} = \sigma^{V}{}_{b}$	Branch
	$\underline{\varepsilon_{ve}{}^{D}{}_{b,elast}}^{mic}$	$\underline{\sigma^{D}{}_{b,elast}}^{mic} = \underline{\sigma^{D}{}_{b}}^{mic}$	microplane branch
	$\varepsilon_{ve}{}^{V}{}_{b,visc}$	$-\sigma^{V}{}_{b,visc} = -\sigma^{V}{}_{b}$	Branch
	$\underline{\varepsilon_{ve}{}^{D}{}_{b,visc}}^{mic}$	$-\underline{\sigma^{D}{}_{b,visc}}^{mic} = -\underline{\sigma^{D}{}_{b}}^{mic}$	microplane branch
Damage	d_V	$-Y_V$	Global
	$d_D{}^{mic}$	$-Y_D{}^{mic}$	Microplane
Viscoplasticity	$\varepsilon_{vp\,s}{}^{V}$	$-\sigma^{V}$	surface / global
	$\underline{\underline{\varepsilon_{vp\,s}{}^{D}}}$	$-\underline{\underline{\sigma^{D}}}$	surface / global
	$\underline{\underline{\xi_s}}$	$\underline{\underline{X_s}}$	Surface

Table 2. *Summary of the state variables and their associated variables defined in the model. The corresponding mechanism and the level of definition of each variable are given.*

3.1.3. Global rheological scheme

Finally, the model corresponds to the rheological diagram in **figure 9**.

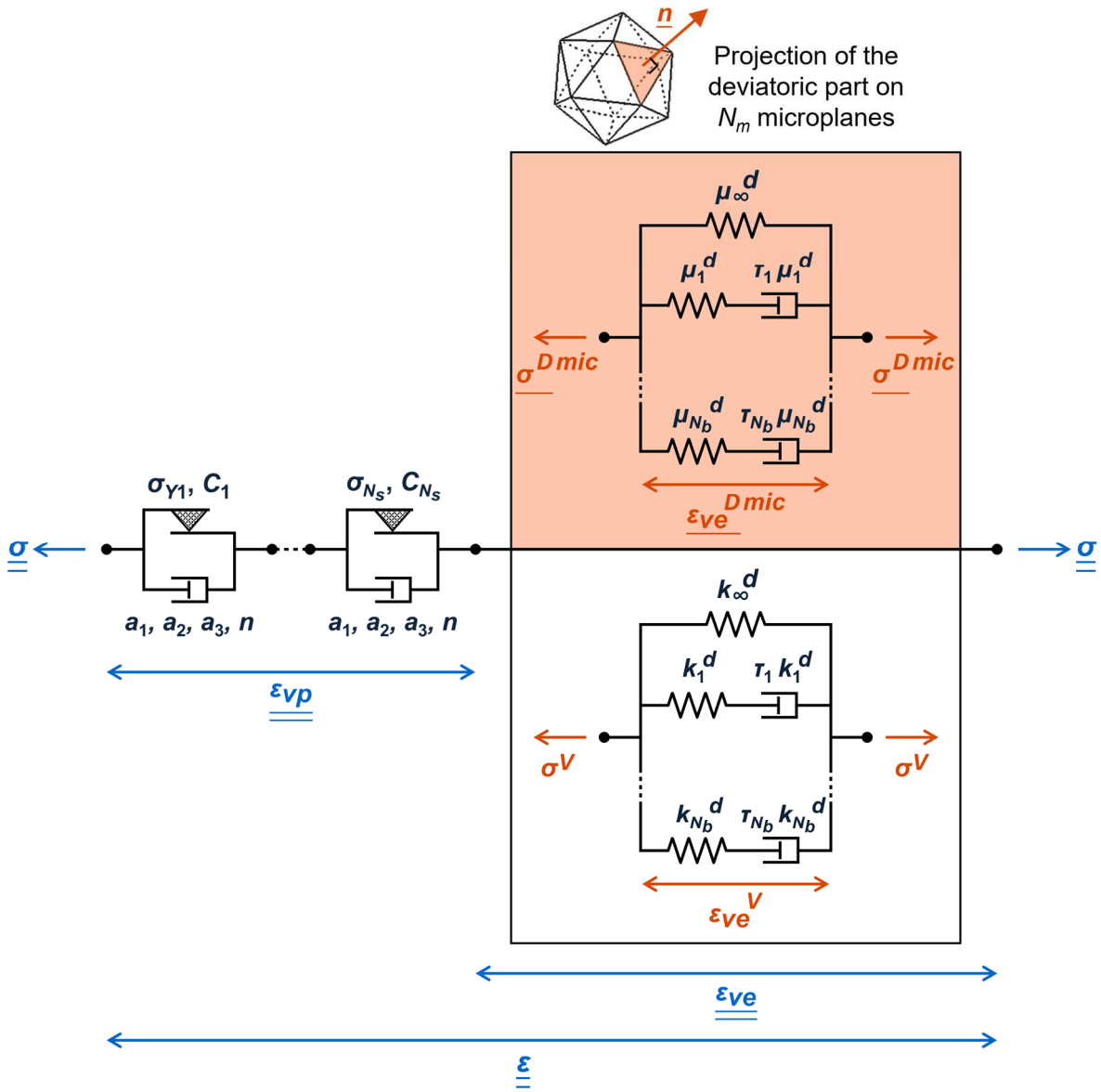

Figure 9. *Rheological diagram of the constitutive law. The elastic modules k_b^d and μ_b^d correspond to the damaged volumetric and deviatoric elastic modules: $k_b^d = (1\text{-}\alpha_{Vb} d_V)\, k_{Vb}$ and $\mu_b^d = (1\text{-}d_D^{mic})\mu_{Db}$. The terms τ_b correspond to the characteristic viscoelastic times.*

3.1.4. Failure criteria

In addition to the data from uniaxial compression and tensile tests, the results of multiaxial tests (Brazilian test, channel-die, equibiaxial compression, torsion) make it possible to identify an asymmetric failure criterion in tensile and compression. To do so, two independent failure criteria must be used. It turns out that the failure criterion developed for the material M1 (Caliez et al. 2014 ; Picart and Pompon, 2016) is perfectly suited to the material M2. The first criterion is based on the critical value of the maximum effective positive principal stress. Stress states as biaxial tensile conditions, tensile test, shear loading, and Brazilian experiments can be predicted by the first criterion. The second criterion relates the maximum positive principal strain to the pressure. It enables predicting loading conditions as uniaxial and triaxial compressions, channel-die tests and equibiaxial compressions. These thresholds are not discussed here. The reader must refer to Picart and Pompon, (2016) for more details.

3.2. Implementation

The model is implemented in incremental form as an Abaqus UMAT subroutine as illustrated in **figure 10** (Plassart, 2020b). The principle of the resolution is as follows. As input to the UMAT, the variables at the time t and the strain increment $\Delta\underline{\underline{\varepsilon}}$ between t and $t+\Delta t$ are known. The UMAT calculates the evolution of the variables over the time increment and the constitutive Jacobian. Abaqus then computes the strain increment for the next step.

The UMAT code has two parts: the viscoelastic one and the viscoplastic one. At the beginning of a time increment (time $t+\Delta t$), a viscoelastic prediction is formulated. The predictor/corrector methodology is a standard approach for integrating ordinary differential equations. For example, see Doghri (1993). The viscoelastic differential equations 5 are integrated at times t and $t+\Delta t$ to express the stress increments $\Delta\sigma^V{}_b$ and $\Delta\underline{\underline{\sigma^D{}_b}}^{mic}$ of each branch. To do so, the strain rates $\dot{\varepsilon}_{ve}{}^V$ and $\underline{\underline{\dot{\varepsilon}_{ve}{}^D}}^{mic}$ are assumed to be constant over the time interval Δt. This provides an estimate of the total stresses (effective and not). The yield criteria f_s are then tested. If there is no active surface, the prediction is correct. Otherwise, a return mapping algorithm applied to viscoplasticity is run. A viscoplastic correction of the prediction is then made following a Newton-Raphson scheme solved by gaussian elimination. Residues are calculated on the stresses $\tilde{\sigma}^V$ and $\underline{\underline{\tilde{\sigma}}}^D$, and on the viscoplastic multiplier $\dot{\lambda}_s$ ($\Delta\lambda_s/\Delta t$ in incremental form). Then comes a system of corrective equations for these three quantities. It is solved by a gaussian elimination method. From the corrected effective stresses and viscoplastic multiplier, strains and hardening are updated. A new viscoelastic computation leads to new values of stresses. If they correspond to the stresses calculated on the viscoplastic part (within a tolerance), the balance is found. Otherwise, a new correction calculation is started. This scheme is repeated until the balance is found. If this is not the case after thirty iterations, the time interval Δt is divided by four and the calculation on the increment is reset.

Sometimes a surface initially detected as active is no longer active after the viscoplastic correction because the estimate effective stress decreases. In this case, the iteration is restarted without considering this surface in the viscoplastic correction.

To provide the constitutive Jacobian $\dfrac{\partial\Delta\underline{\underline{\sigma}}}{\partial\Delta\underline{\underline{\varepsilon}}}$, we have chosen a numerical computation rather than an analytical one. This Jacobian is determined by a perturbation method of the strain increment tensor. The principle is to determine the stress increment obtained for a perturbation one hundred times smaller than the strain increment $\Delta\underline{\underline{\varepsilon}}$ (a minimum amplitude of the perturbation is guaranteed). This Jacobian is automatically symmetrised by the software.

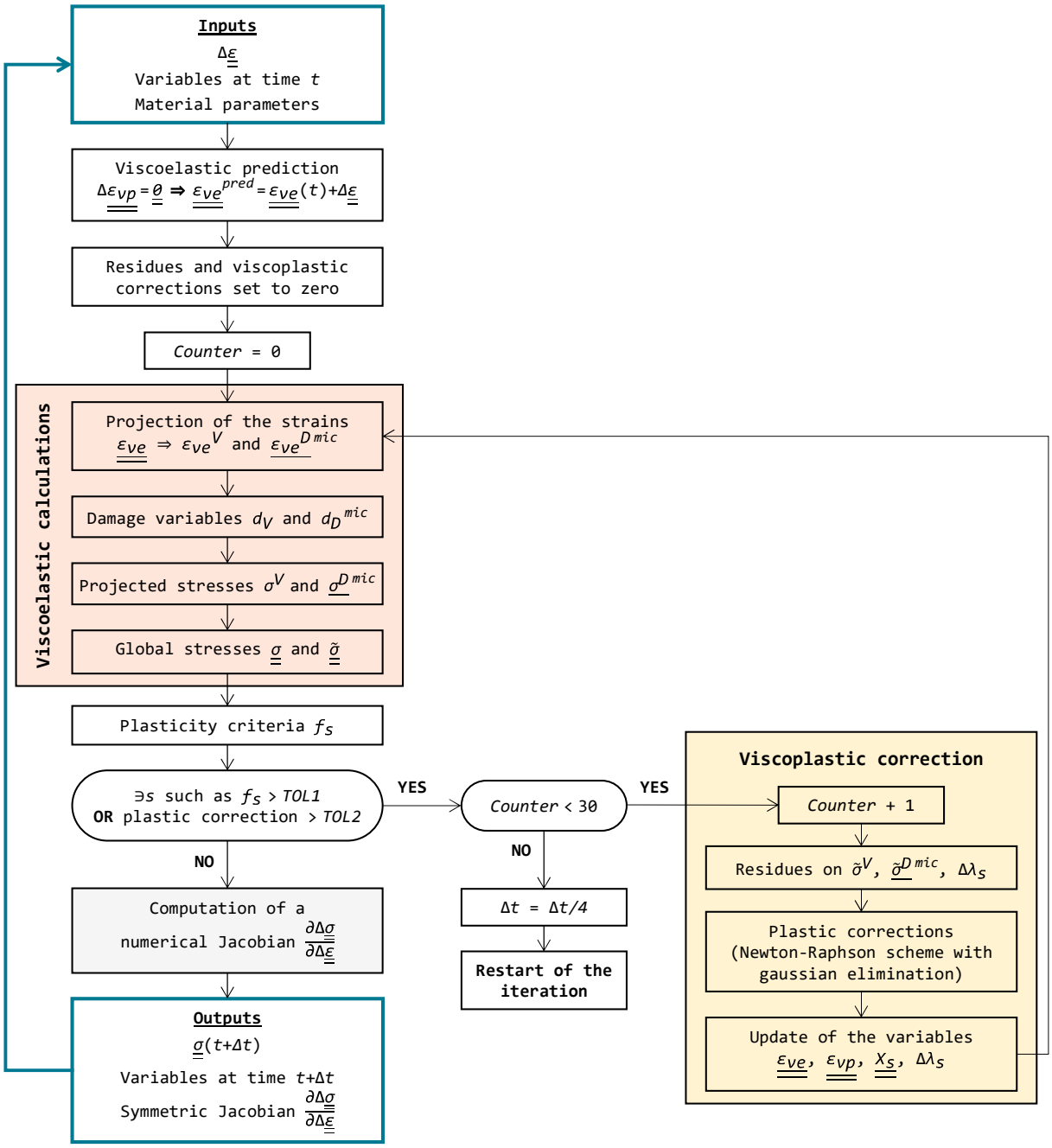

Figure 10. *Algorithm for the integration of the behaviour law in the Abaqus/Standard calculation code.*

3.3. Determining the parameters

The microplanes directions and the corresponding angular weighting coefficients has been calculated by Bažant and Oh (1985) for a discretization of the hemisphere in 21, 33, 37 and 61 directions. For modelling the material M2, 21 microplanes are used.

The parameters of the generalized Maxwell model have been determined by discretizing the master curves at 0°C in fourteen characteristic times. These times and the corresponding longitudinal elastic modules are given in **table 3**. To get the values of the relaxation times at 20°C, the time-temperature equivalence is used. The bulk and shear modules are determined with a Poisson's ratio of 0.35 experimentally measured (Plassart *et al.*, 2020a).

The damage is determined from the degradation of the modules measured in cyclic loading. For M2, the bulk modulus does not decrease. So, there is no volumetric damage. The shear modulus slowly decreased after a given threshold. This modulus being global, it does not enable to highlight the damages for each microplane $d_D{}^{mic}$. Their evolution law is determined by an inverse method. The parameters of the law are fitted to reproduce the degradation of the global shear modulus in uniaxial tensile, uniaxial compression and triaxial compression. This module is not calculated at each stage of the simulation. It is evaluated from the final simulation curve.

A power law triggered by threshold is used:

$$\begin{cases} d_D{}^{mic}(t+\Delta t) = d_{D0} & \text{if } Y_{D\infty}{}^{mic} \le y_{D0} \\ d_D{}^{mic}(t+\Delta t) = \max\left(d_D{}^{mic}(t),\, \min\left(1,\, \xi_{D1}\left(Y_{D\infty}{}^{mic} - y_{D0}\right)^{\xi_{D2}}\right)\right) & \text{if } Y_{D\infty}{}^{mic} > y_{D0} \end{cases} \tag{14}$$

with ξ_{D1} and ξ_{D2} the parameters of the power law and y_{D0} the triggering threshold. Their values are given in **table 4**.

To describe the non-linear viscoplastic flow, nine yield surfaces are chosen. It is the smallest number leading to smooth curves. The yield strength and the hardening modulus of each surface have been set to reproduce the experimental relaxed stress points in cyclic compression. The selected values are given in **table 5**.

The objective of the viscoplastic calibration is double. The global stress level (envelope curve) must be reached, and the viscous flow (relaxation and recovery times) must be reproduced. In the viscoplastic flow law (equation 10), the power function (parameter a_1) manages the small flows (low levels of f_s) and the time evolution of the stress relaxation. The exponential function (parameters a_2 and a_3) manages the larger levels of f_s and the pressure dependence. The parameter n appearing in both functions manages their weighting. The parameters are given in **table 6**. They have been calibrated from a cyclic compression test. The monotonic compression at 10 MPa pressure has been used to identify the parameter a_3.

A single dilatancy function is chosen. It regulates the ratio between the volumetric and deviatoric flows of each yield surface (equation 9) as follows:

$$\beta = \frac{\dot{\varepsilon}_{vp}{}^{V}}{\sum_s \left| \underline{\underline{\dot{\varepsilon}_{vp\,s}}}^{D} \right|} \tag{15}$$

To estimate the experimental viscoplastic strains developed during a test, a model without plasticity has been implemented. The viscoelastic parameters and the damage law are those described above. The test is simulated and compared to experimental data. Viscoelasticity and viscoplasticity additively acting in the model, the “experimental” viscoplastic strains are the difference between the total experimental strains and the viscoelastic simulated strains. However, the experimental data only enable accessing the norm of the total viscoplastic strains. In monotonic proportional loading, the loading surfaces all have the same direction and the rates $\underline{\underline{\dot{\varepsilon}_{vp\,s}}}^{D}$ have the same sign. The equality $\left| \sum_s \underline{\underline{\dot{\varepsilon}_{vp\,s}}}^{D} \right| = \sum_s \left| \underline{\underline{\dot{\varepsilon}_{vp\,s}}}^{D} \right|$ is then verified. The dilatancy function β has been determined on the monotonic proportional loading tests (uniaxial and triaxial compressions, uniaxial traction, torsion):

$$\begin{aligned} \beta = {} & \beta_{t1}\, \langle \tilde{\sigma}^V \rangle_+ \left(1 - \exp\left(-\beta_{t2} \left| \underline{\underline{\varepsilon_{vp}}}^{D} \right| \right) \right) \\ & + \tanh\left(\beta_{c1} \langle \tilde{\sigma}^V \rangle_- \right) \left(\beta_{c2} + \beta_{c3} \tilde{\sigma}^V - \beta_{c4} \exp\left(-\beta_{c5} \left| \underline{\underline{\varepsilon_{vp}}}^{D} \right| \right) - \beta_{c6} \exp\left(-\beta_{c7} \left| \underline{\underline{\varepsilon_{vp}}}^{D} \right| \right) \right) \end{aligned} \tag{16}$$

The terms $\langle \tilde{\sigma}^V \rangle_+$ and $\tanh\left(\beta_{c1} \langle \tilde{\sigma}^V \rangle_- \right)$ describe a continuous function, null at zero pressure, with two different expressions in tensile and compression. The β_{ti} and β_{ci} are parameters. They are given in **table 7**.

Branch	∞	1	2	3	4	5	6	7	8	9	10	11	12	13	14
$\tau_{ref\ b}$ (s)	/	10^{-2}	10^{-1}	1	10	10^{2}	10^{3}	10^{4}	10^{5}	10^{6}	10^{7}	10^{8}	10^{9}	10^{10}	10^{11}
E_b (MPa)	4480	140	100	110	110	120	130	140	150	220	380	550	840	710	1

Table 3. *Values of relaxation times and longitudinal elastic modules for a reference temperature of 0°C.*

y_{D0} (MPa)	ξ_{D1} (MPa^{-1})	ξ_{D2}
$7x10^{-3}$	12	1.4

Table 4. *Values of the parameters of the damage law.*

Surface *s*	1	2	3	4	5	6	7	8	9
σ_{Ys} (MPa)	1	6	11	15	18	20	22	23	23.5
C_s (MPa)	15000	11000	8000	4500	3000	2000	500	100	1

Table 5. *Values of the yield strength and kinematic strain hardening modulus.*

n	a_1 (s^{-1}.MPa)	a_2 (MPa^{-n-1})	a_3 (MPa^{-n-2})
2	$3.0x10^{4}$	$1.3x10^{-2}$	$-5.3x10^{-2}$

Table 6. *Values of the parameters of the viscoplastic law.*

β_{t1}	β_{t2} (MPa^{-1})	β_{c1} (MPa^{-1})	β_{c2}	β_{c3} (MPa^{-1})	β_{c4}	β_{c5}	β_{c6}	β_{c7}
0.2	$60x10^{3}$	10^{6}	7.4	$1.5x10^{-2}$	7.25	2.4	0.5	960

Table 7. *Values of the parameters of the dilatancy function.*

4. Results and discussion

The simulations have been performed using the Abaqus/Standard finite element code on a C3D8 element (unless otherwise stated). Symmetry constraints were imposed on three faces of respective normal x, y, and z. Small time steps were used to describe the non-linearity (a monotonic compression curve has about 100 points). The step time independence of the results has been verified. In the following figures, the experimental data are in black. The simulations of tests used for the determination of the parameters are in blue. The simulations of the other tests are in red. This colour code does not apply to the simulation of 0°-0° and 0°-90° compressions.

First, the model is tested in cyclic uniaxial compression test at $1.7x10^{-5}$ s^{-1} (the reference strain rate). The simulation (envelope curve and hysteresis) is close to the experimental data (**figure 11**). The longitudinal strains levels are excellent. The dilatancy is well reproduced, although it is a little too large when the unloadings end (upper graph **figure 11**). Remind that the dilatancy was parameterized on monotonic tests. All loading and unloading elastic modules are reproduced. The amplitude of the relaxation and recovery phases is good. The lower graphs (**figure 11**) show the time versus the strain recovery on the first two graphs and versus the stress relaxation on the last one. Flow is reproduced along time.

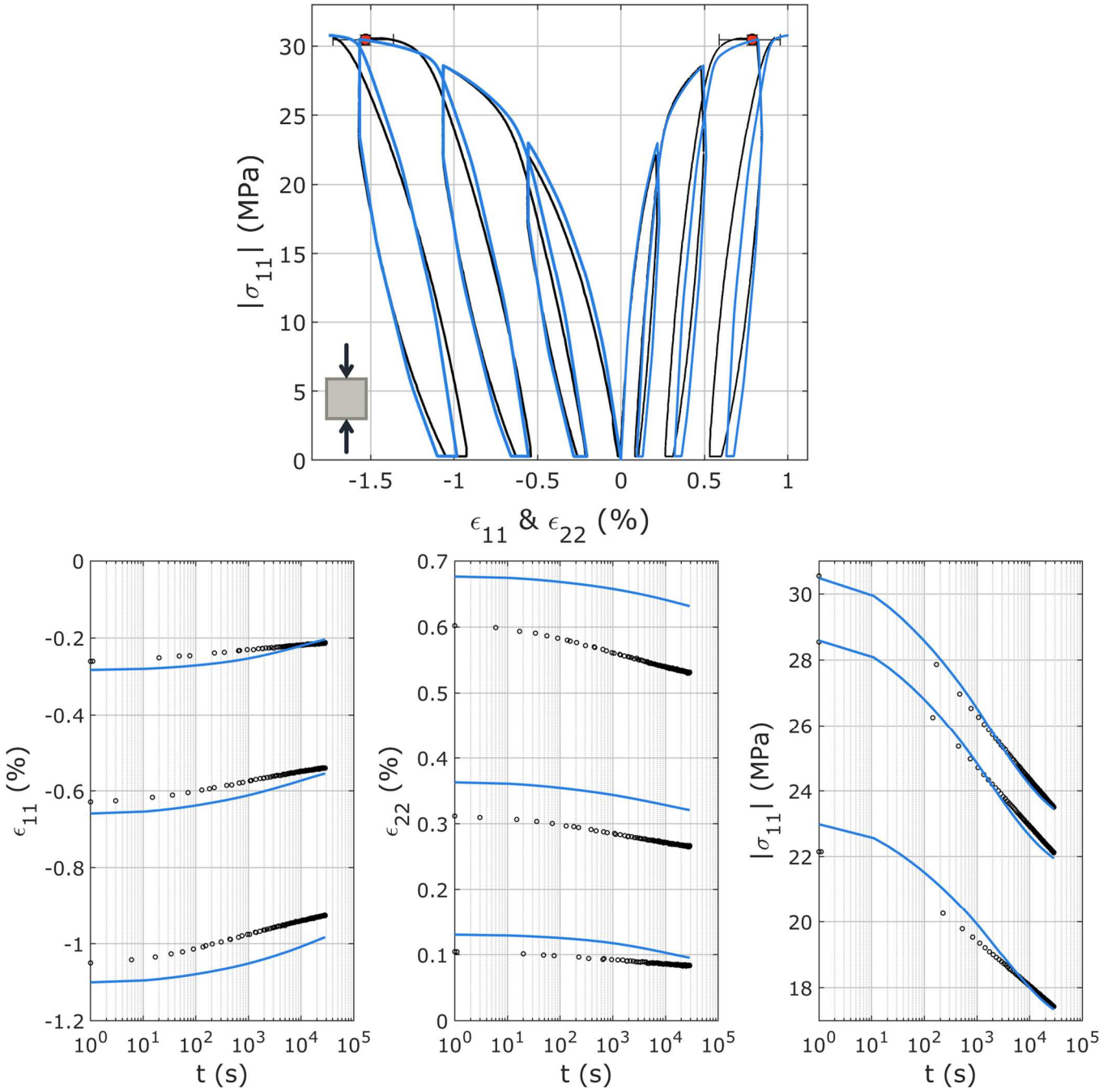

Figure 11. *Simulation of a cyclic uniaxial compression test performed at 1.7x10^{-5} s^{-1}. The bottom figures present the strain recoveries and the stress relaxations. The experimental data are in black. This simulation, used to calibrate the parameters, is in blue.*

The rate effect of the model was tested in uniaxial compression (**figure 12**) and tensile (**figure 13**). **Figure 12** shows that the maximum stress in compression at 1.7x10^{-6} s^{-1} is slightly underestimated and good at 1.7x10^{-4} s^{-1}. In tensile, **figure 13**, the overall behaviour lacks non-linearity, but the strain and stress levels are correct. The shape of the tensile curves is related to the parameter a_1 of the viscoplastic flow. a_1 controlling the flow in relaxations and recoveries as well as in tensile, a compromise was found here.

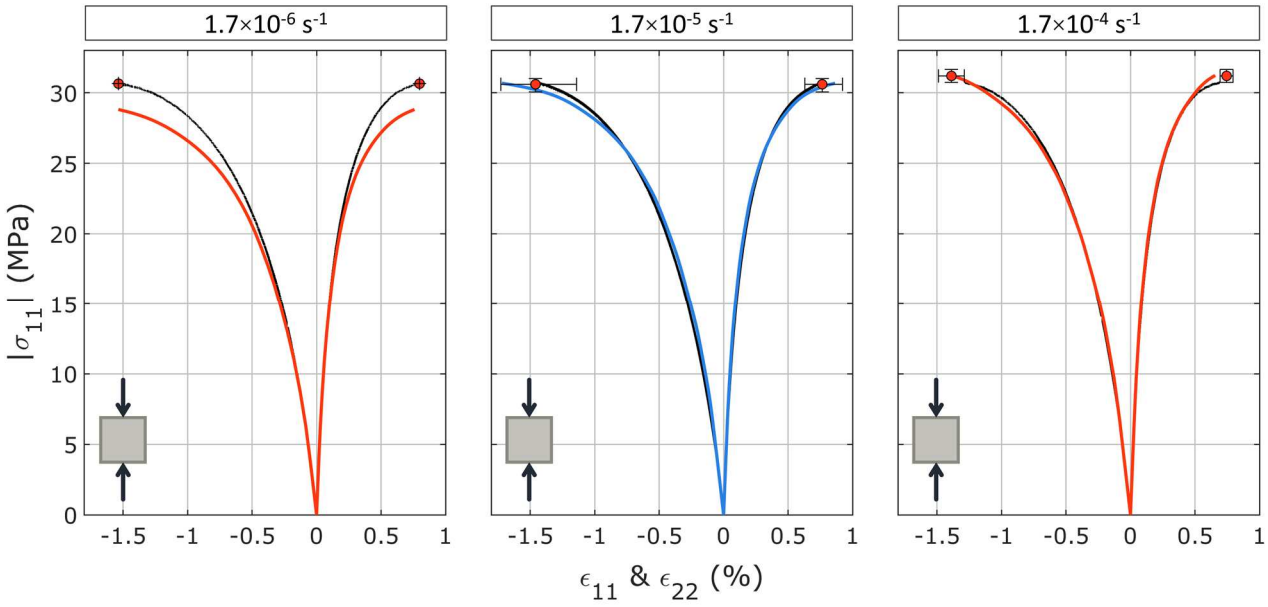

Figure 12. *Simulation of the monotonic uniaxial compression tests performed at the three strain rates. The experimental data are in black. The simulation at 1.7x10^{-5} s^{-1}, which has been used to calibrate the dilatancy, is in blue. The two others simulations are in red.*

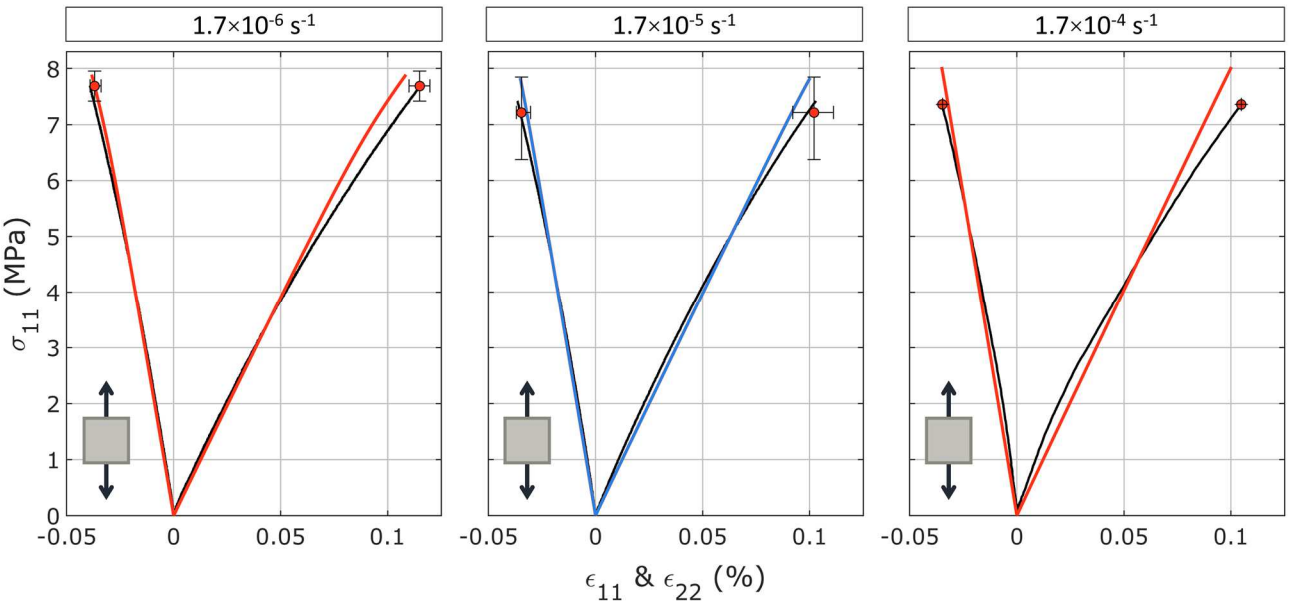

Figure 13. *Simulation of the monotonic uniaxial tensile tests performed at the three strain rates. The experimental data are in black. The simulation at 1.7x10^{-5} s^{-1}, which has been used to calibrate the dilatancy, is in blue. The two others simulations are in red.*

The dilatancy and the pressure effect have been calibrated on the monotonic triaxial tests, and the model correctly reproduces these tests. The **figure 14** presents the simulation of a cycling compression under a confinement of 10 MPa. The envelope behaviour is well simulated. However, the relaxation amplitude is a little too high. Furthermore, the unloads are too stiff which leads to excessive residual strains. For reminder, the viscoplastic flow depends on pressure. In future work, a dependence of the strain hardening modules to the pressure could be add. At a given stress level, the hardening modules seems too low since there is too much flow during relaxation.

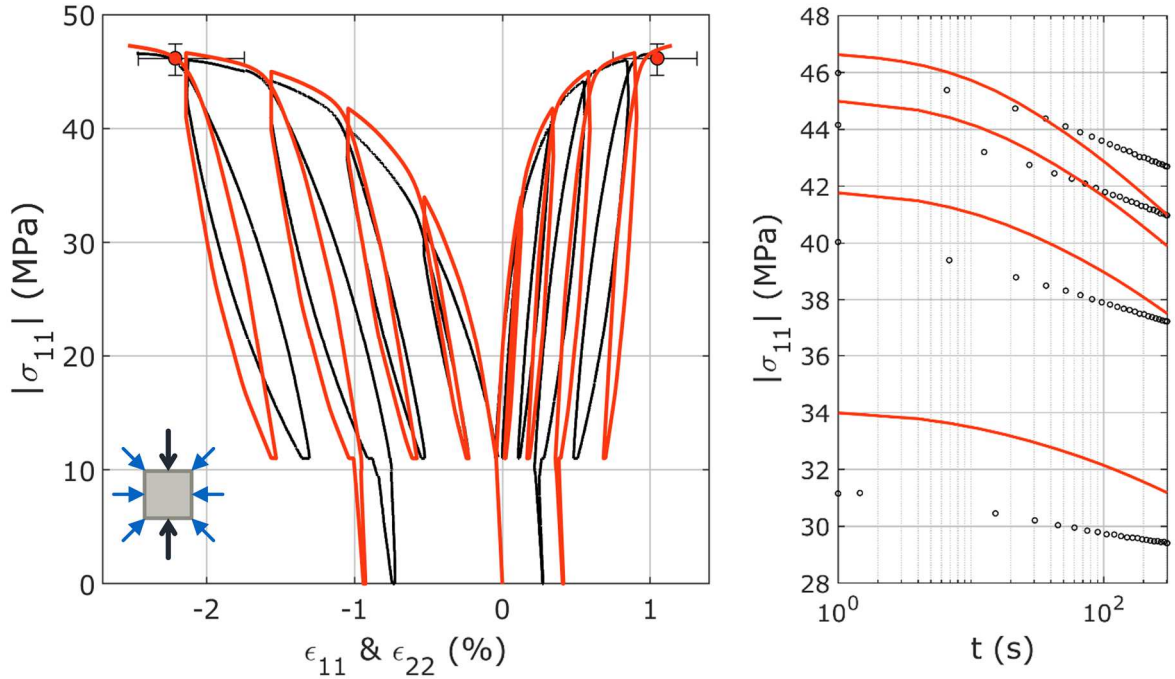

Figure 14. *Simulation of the cyclic triaxial compression test performed at 1.7x10^{-5} s^{-1} at 10 MPa pressure. The right figure presents the stress relaxations. The experimental data are in black. The simulation is in red.*

Since the torsion test is a heterogeneous one, a modelling of the experimental set-up has been made. The sample is embedded between two plates (**figure 15** left). The bottom one is fixed, the top one applies the torque. The strains are those of a node at the centre of the sample on the outer radius ("measuring point" on the scheme). This corresponds to the place where the gauges were experimentally glued. The comparison between the simulation and the three tests performed shows a good fit of the model (**figure 15** right). The alternating torsion test, twenty times cycled (**figure 6**), has also been simulated. As experimentally, the model is accommodated from the second cycle.

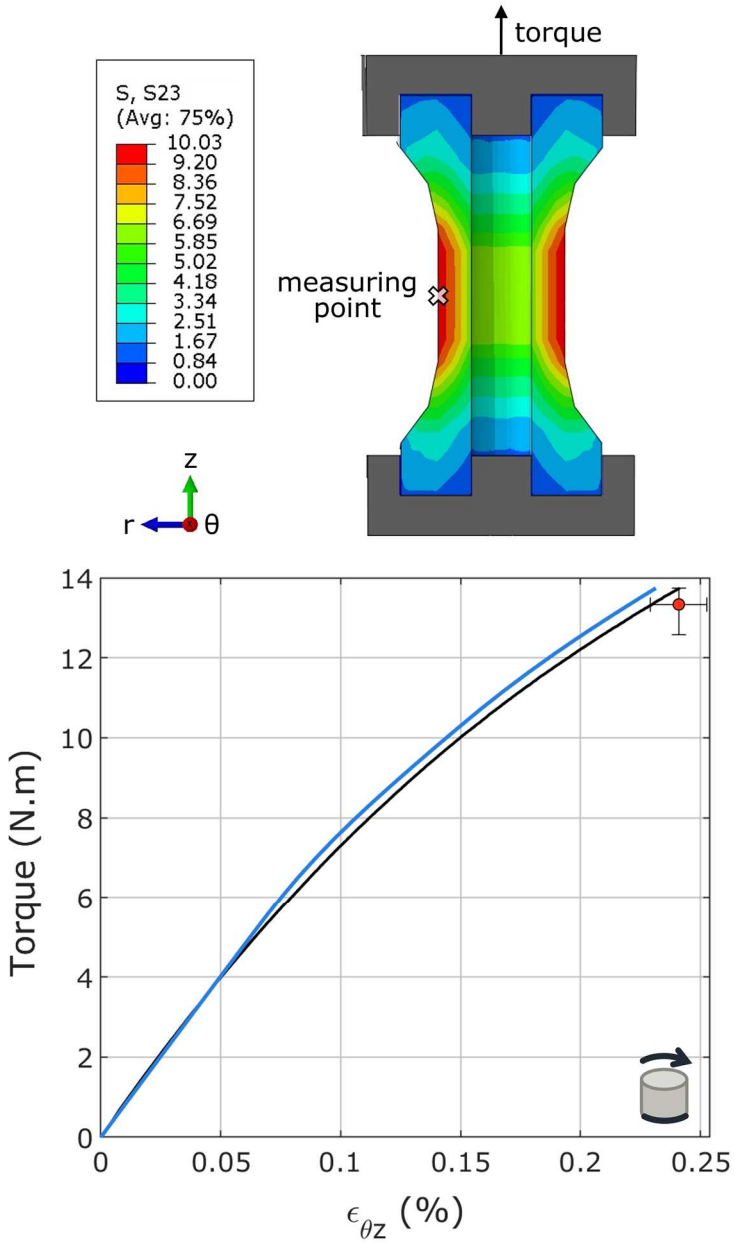

Figure 15. *Simulation of the monotonic torsion test performed at 0.015°s^{-1}. The stress S23 (corresponding to rθ-plane) is expressed in MPa. The experimental data, which has been used to calibrate the dilatancy, are in black. The tests dispersion is shown by the error bar. The simulation is in blue.*

The 0°-0° and 0°-90° compression tests gave information to choose the kind of hardening. Their simulation highlights the behaviour of the material is well understood (**figure 16**). The model reproduces the experimental mechanisms: a compression stiffens the longitudinal direction of the load and softens the transversal one; the unloadings behave like a reloading at 0°.

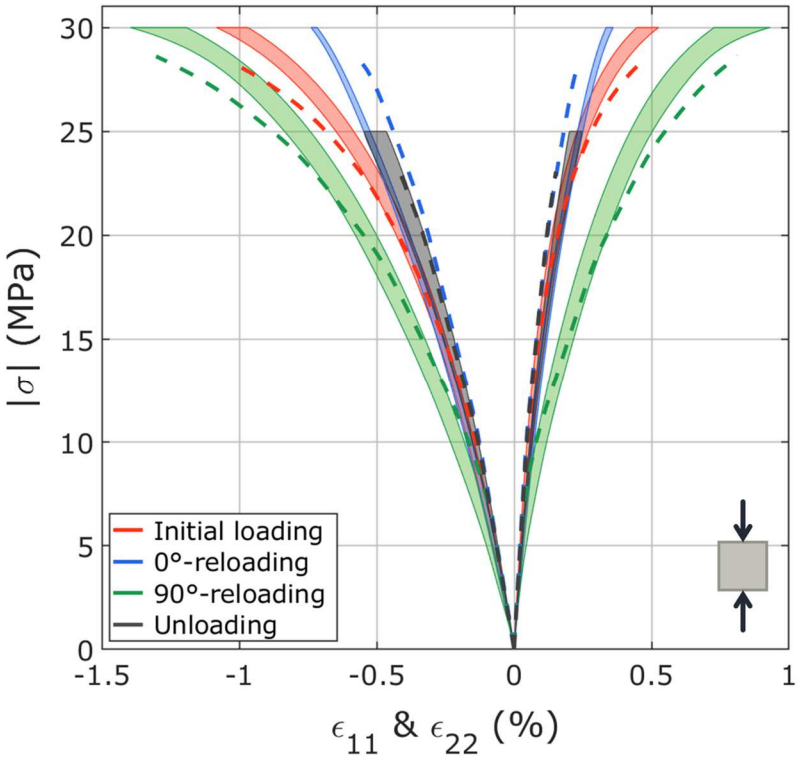

Figure 16. *Simulation of the 0°-0° and 0°-90° compression tests. The experimental data are the surfaces. The simulations are the dotted lines. These tests were not used to parameterize the model. The initial loadings are in red. The 0° reloading is in blue. The 90° reloading is in red. The unloadings are in grey.*

At last, the subroutine has been evaluated under multiaxial loading. The channel-die test and the equibiaxial compression (described in Plassart *et al.*, 2020a) have been simulated. The results, shown **figure 17**, are positive. The experimental data are very noisy (poor quality of image correlation), but the model describes the trend.

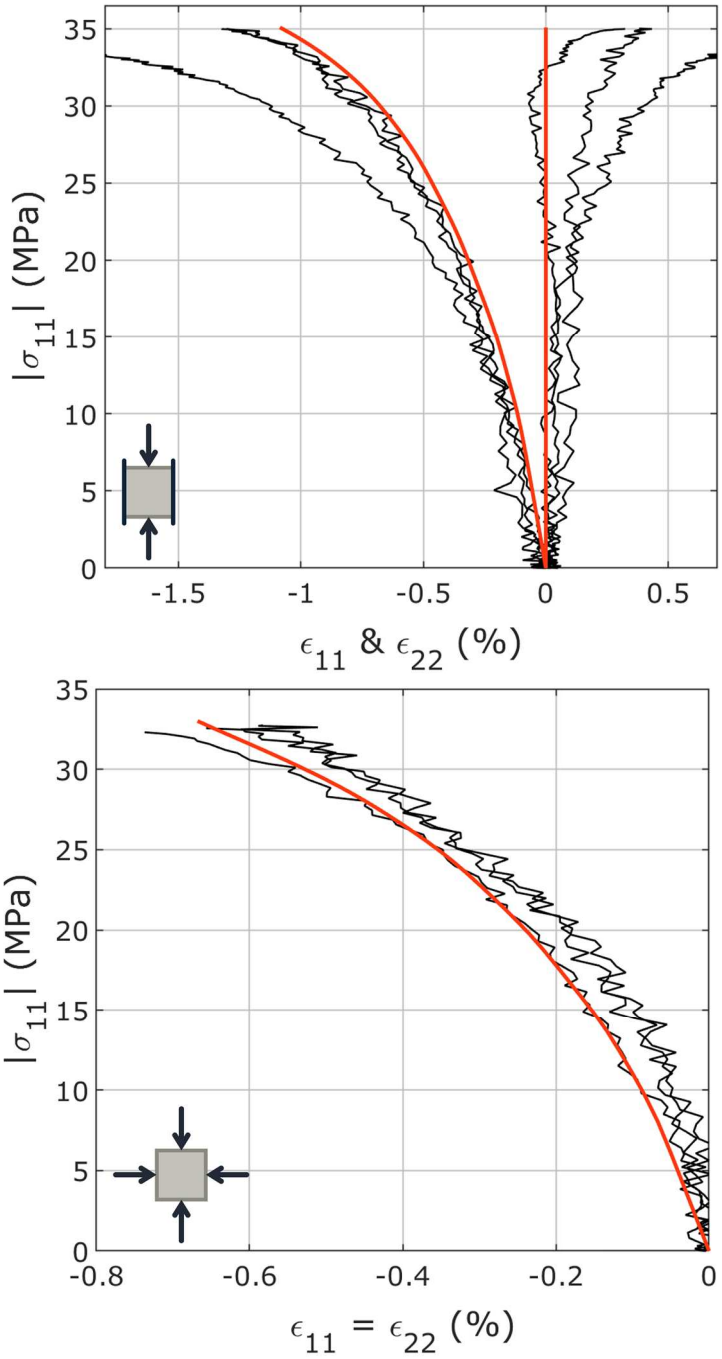

Figure 17. *Simulation of the channel-die test on the top, and of the equibiaxial compression on the bottom. The experimental data are in black (three tests of each). The simulations are in red.*

Finally, the model calibrated on M2 can reproduce about ten experimental loading paths in the principal stress space. These loading paths are plotted **figure 18**. In this graph, the principal stresses are sorted in descending order (σ_I>σ_{II}>σ_{III}). A compression has a negative sign while a traction as a positive one. Torsions are in the (σ_I;σ_{II}) plane. Channel-die tests and equibiaxial compressions are in the (σ_{II};σ_{III}) plane. The recompression at 90° (in light blue) follows a uniaxial compression (in dark blue).

In addition of these loading paths, the rate-dependence has been considering in the model: three strain rates in compression and tensile plus slowest rates in relaxation and recovery. About the integration of the temperature dependence, the reader is invited to read Plassart (2020b).

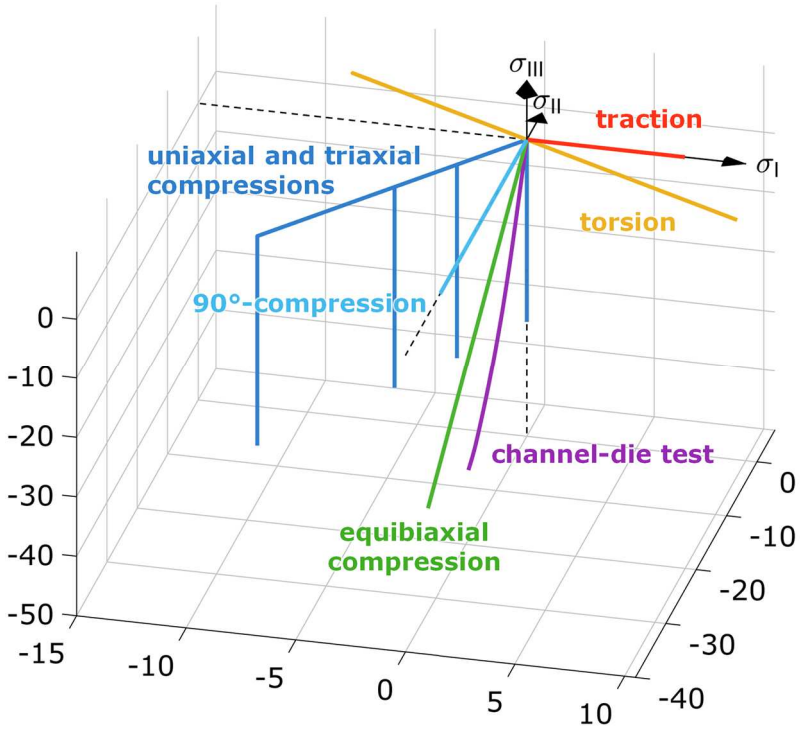

Figure 18. *Representation in the space of the three principal stresses of the loading paths performed experimentally on M2 and reproduced by the model. In this graph, $\sigma_I > \sigma_{II} > \sigma_{III}$. A compression has a negative sign while a traction as a positive one.*

5. Conclusion

Nowadays, ensuring the safety and reliability of pyrotechnic structures is done by numerical simulations. The explosive composition must be accurately modelled. A recent exhaustive state of the art of quasistatic mechanical tests shown that few experimental campaigns have been carried out on energetic materials (except for an HMX-based material, the explosive composition M1), resulting in many assumptions about their behaviour. To fill the gap on TATB-based PBXs, an exhaustive characterization of M2 was provided by the authors. This database includes atypical tests (multiaxial, cyclic, alternated) with transversal strains measurements, which enables understanding the behaviour of M2. The key features of the behaviour of M2, close to that of M1, has been recall in this paper: strain rate-, temperature- and pressure-dependence, inelastic strain, and a load-induced anisotropy. The main deformation mechanism of M2 is the non-associated viscoplastic flow with kinematic strain hardening. This material develops few damages. In contrast, the load-induced anisotropy of M1 was attributed to damage. Since HMX- and TATB-based PBXs have similar macroscopic properties, a single constitutive law is attainable for this class of materials. The mechanisms implemented would be the same, each explosive composition having its own set of parameters.

Because of the lack of experimental study, the already proposed constitutive laws are based on many assumptions. None of these models describes all the deformations mechanisms of the PBXs. Therefore, a new constitutive law has been proposed in this paper. The proposed model has a damageable viscoelastic component in series with a non-associated viscoplastic component. There are two sources of load-induced anisotropy: anisotropic damage and kinematic strain hardening. The pressure-dependence has been integrated in the viscoplastic flow law. A calibration has been proposed for the explosive composition M2.

The law has been implemented as a UMAT subroutine for Abaqus/Standard. The tests from the experimental database have been simulated for comparison. There is a good agreement between the experimental data and the simulations whatever the loading path and the strain rate. The simulation of non-proportional loadings (0°-90° compression and channel-die test) give satisfactory results.

Since this model incorporates damage-induced anisotropy, modelling the behaviour of other PBXs would be possible. Future work will focus on applying it to M1. This will require a new identification of the model parameters.

However, several improvements have been pointed out. To describe the non-associated flow, a dilatancy function has been defined. It has been determined in monotonic loadings, but its calibration is not optimal in unloading. In addition, this function has nine parameters. Furthermore, in the absence of experimental information, we have chosen to integrate the pressure effect only on the viscoplastic flow law. The simulation of the cyclic triaxial compression at 10 MPa pressure shows an excess of stress relaxation. A pressure-dependence to the strain hardening parameters could be incorporated to the model. The confinement would increase the yield stress or/and the hardening modules and so the relaxed stresses.

6. Acknowledgements

This work has been carried out within the framework of the research program of the Corresponding Research Laboratory (CosMa), a joint laboratory combining CEA Le Ripault and the Gabriel LaMé Mechanical laboratory.

7. References

Ambos A., Willot F., Jeulin D., Trumel H. (2015) – Numerical modeling of the thermal expansion of an energetic material. *International Journal of Solids and Structures, 60-61. https://doi.org/10.1051/mattech/2015019.*

Armstrong P.J., Frederick C.O. (1966) – A mathematical representation of the multiaxial Bauschinger effect. *Central Electricity Generating Board [and] Berkeley Nuclear Laboratories, Research & Development Department.*

Armstrong P.J., Frederick C.O. (2007) – A mathematical representation of the multiaxial Bauschinger effect. *Materials at High Temperatures, 24(1). https://doi.org/10.1179/096034007X207589.*

Arora H., Tarleton E., Li-Mayer J., Charalambides M.N., Lewis D. (2015) – Modelling the damage and deformation process in a plastic bonded explosive microstructure under tensile using the finite element method, *Computational Materials Science, 110. https://doi.org/10.1016/j.commatsci.2015.08.004.*

Bažant Z.P., Oh B.H. (1985) – Microplane model for progressive fracture of concrete and rock. *Journal of Engineering Mechanics, 111(4). https://doi.org/10.1061/(ASCE)0733-9399(1985)111:4(559).*

Benelfellah A. (2013) – Contribution à la modélisation de l'anisotropie induite par endommagement d'un matériau agrégataire énergétique. *PhD thesis. https://hal.archives-ouvertes.fr/tel-02966078/.*

Benelfellah A., Frachon A., Gratton M., Caliez M., Picart D. (2014) – Analytical and numerical comparison of discrete damage models with induced anisotropy. *Engineering Fracture Mechanics, 121/122. https://doi.org/10.1016/j.engfracmech.2014.03.022.*

Benelfellah A., Frachon A., Gratton M., Caliez M., Picart D. (2017) – VDT microplane model with anisotropic effectiveness and plasticity. *Mechanics & Industry, 18(607). https://doi.org/10.1051/meca/2017032.*

Bennett J.G., Haberman K.S., Johnson J.N., Asay B.W., Henson B.F. (1998) – A constitutive model of the non-shock ignition and mechanical response of high-explosives. *Journal of the Mechanics and Physics of Solids, 46. https://doi.org/10.1051/meca/2017032.*

Benouniche S. (1979) – Modélisation de l'endommagement du béton par microfissuration en compression. *PhD thesis.*

Buechler M.A. (2012a) – Observed physical processes in mechanical tests of PBX 9501 and recommendations for experiments to explore a possible plasticity/damage threshold. *Los Alamos National Laboratory, rapport n° LA-UR-12-21072. https://www.osti.gov/servlets/purl/1039687.*

Buechler M.A. (2012b) – Viscoelastic-viscoplastic combined hardening constitutive model based on the Drucker-Prager yield and flow potentials. *Los Alamos National Laboratory, rapport n° LA-UR-12-24895. https://www.osti.gov/servlets/purl/1052364.*

Buechler M.A. (2013) – Viscoelastic-viscoplastic damage model development, parameters estimation, and comparison to PBX9501 experimental data. *Los Alamos National Laboratory, rapport n° LA-UR-13-DRAFT. https://www.osti.gov/servlets/purl/1095206.*

Caliez M., Gratton M., Frachon A., Benelfellah A., Picart D. (2014) – Viscoelastic plastic model and experimental validation for a granular energetic material. *International Journal of Energetic Materials and Chemical Propulsion, 13. https://doi.org/10.1016/j.engfracmech.2014.09.009.*

Cambou B., Lanier J. (1988) – Induced anisotropy in cohesionless soil: experiments and modelling. *Computers and Geotechnics, 6. https://doi.org/10.1016/0266-352X(88)90071-7.*

Carol I., Jirásek M., Bažant Z. (2001) – A thermodynamically consistent approach to microplane theory. Part I: Free energy and consistent microplane stresses. *International journal of solids and structures, 38(17). https://doi.org/10.1016/S0020-7683(00)00212-2.*

Chaboche J.L., Dang Van K., Cordier G. (1979) – Modelization of the strain memory effect on the cyclic hardening of 316 stainless steel. *Transactions of the 5th International Conference of SMiRT, Berlin.*

Chatti M., Frachon A., Gratton M., Caliez M., Picart D., Aït Hocine N. (2019) – Modelling of the viscoelastic behaviour with damage induced anisotropy of plastic-bonded explosive based on the microplane approach. *International Journal of Solids and Structures, 168. https://doi.org/10.1016/j.ijsolstr.2018.08.018.*

Chiarelli A.S. (2000) – Étude expérimentale et modélisation du comportement mécanique de l'argilite de l'Est : influence de la profondeur et de la teneur en eau. *PhD thesis. https://www.theses.fr/2000LIL10072.*

Clements B.E., Mas E.M. (2004) – A theory for plastic-bonded materials with a bimodal size distribution of filler particles. *Modelling and Simulation in Materials Science and Engineering, 12. https://doi.org/10.1088/0965-0393/12/3/004.*

Dasriaux M. (2013) – Évolutions microstructurales du PEEK au-dessus de sa température de transition vitreuse lors de maintiens sous pression et température. *PhD thesis. https://tel.archives-ouvertes.fr/tel-00786016.*

Desmorat R., Cantournet S. (2008) – Modeling microdefects closure effect with isotropic/anisotropic damage. *International Journal of Damage Mechanics, 17(1). https://doi.org/10.1177/1056789507069541.*

Dienes J.K. (1978) – A statistical theory of fragmentation. *Proceedings of 19th US Rock Mechanics Symposium, University of Nevada. https://permalink.lanl.gov/object/tr?what=info:lanl-repo/lareport/LA-UR-78-0616.*

Dienes J.K. (1996) – A unified theory of flow, hot-spots, and fragmentation with an application to explosive sensitivity. *High Pressure Shock Compression of Solids II, Springer. https://doi.org/10.1007/978-1-4612-2320-7_14.*

Dienes J.K., Zuo Q.H., Kershner J.D. (2006) – Impact initiation of explosives and propellants via statistical cracks mechanics. *Journal of the Mechanics and Physics of Solids, 54. https://doi.org/10.1016/j.jmps.2005.12.001.*

Doghri I. (1993) – Fully implicit integration and consistent tangent modulus in elasto-plasticity. *International journal for numerical methods in engineering, 36(22). https://doi.org/10.1002/nme.1620362210.*

Gasnier J.B., Willot F., Trumel H., Jeulin D., Biessy M. (2018) – Thermoelastic properties of microcracked polycrystals. Part II: The case of jointed polycrystalline TATB. *International Journal of Solids and Structure, 155. https://doi.org/10.1016/j.ijsolstr.2018.07.025.*

Gotuwka V. (1999) – Étude expérimentale du comportement mécanique des bétons à très hautes performances sous sollicitations multiaxiales simples et complexes. *PhD thesis. https://ori-nuxeo.univ-lille1.fr/nuxeo/site/esupversions/19bee463-ede4-40f3-91cd-f6a018ce16be.*

Gratton M., Gontier C., Rja Fi Allah S., Bouchou A., Picart D. (2009) – Mechanical characterisation of a viscoplastic material sensitive to hydrostatic pressure. *European Journal of Mechanics A/Solids, 28(5). https://doi.org/10.1016/j.euromechsol.2009.03.002.*

Green S.J., Swanson S.R. (1973) – Static constitutive relations for concrete. *Air Force Weapons Laboratory, rapport technique n°AFWL-TR-72-244. https://apps.dtic.mil/sti/pdfs/AD0761820.pdf.*

Hackett R.M., Bennett J.G. (2000) – An implicit finite element material model for energetic particulate composite materials. *International Journal for Numerical Methods in Engineering, 49(9). https://doi.org/10.1002/1097-0207(20001130)49:9<1191::AID-NME997>3.0.CO;2-V.*

Homand-Etienne F., Hoxha D., Shao J.F. (1998) – A Continuum Damage Constitutive Law for Brittle Rocks. *Computers and Geotechnics, 22(2). https://doi.org/10.1016/S0266-352X(98)00003-2.*

Hu D.W., Zhou H., Zhang F., Shao J.F. (2010) – Evolution of poroelastic properties and permeability in damaged sandstone. *International Journal of Rock Mechanics and Mining Sciences, 47. https://doi.org/10.1016/j.ijrmms.2010.06.007.*

Lanier J., Di Prisco C., Nova R. (1991) – Étude expérimentale et analyse théorique de l'anisotropie induite du sable d'Hostun. *Revue Française de Géotechnique, 57. https://doi.org/10.1051/geotech/1991057059.*

Le V.D. (2007) – Modélisation et identification du comportement plastique visco-élastique endommageable d'un matériau. *PhD thesis. https://www.theses.fr/2007TOUR4044.*

Le V.D., Gratton M., Caliez M., Frachon A., Picart D. (2010) – Experimental mechanical characterization of plastic-bonded explosives. *Journal of Materials Science, 45(21). https://doi.org/10.1007/s10853-010-4655-5.*

Lemaître J., Chaboche J.L., Benallal A., Desmorat R. (2020) – Mécanique des matériaux solides, 3e édition. *Editions Dunod.*

Leukart M., Ramm E. (2002) – An alternative split within the microplane material model. *Proceedings of the 5th World Congress on Computational Mechanics.*

Leukart M., Ramm E. (2003) – A comparison of damage models formulated on different material scales. *Computational Materials Science, 28(3-4). https://doi.org/10.1016/j.commatsci.2003.08.029.*

Liénard C. (1989) – Plasticité couplée à l'endommagement en conditions quasi-unilatérales pour la prévision de l'amorçage des fissures. *PhD thesis. http://www.theses.fr/1989PA066317.*

Liu M., Huang X.C., Wu Y.Q., Chen C.J., Huang F.L. (2019) – Numerical simulations of the damage evolution for plastic-bonded explosives subjected to complex stress states. *Mechanics of Material, 139. https://doi.org/10.1016/j.mechmat.2019.103179.*

Mazars J., Berthaud Y., Ramtani S. (1990) – The unilateral behaviour of damaged concrete. *Engineering Fracture Mechanics, 35(4/5). https://doi.org/10.1016/0013-7944(90)90145-7.*

Montáns F.J. (2000) – Implicit algorithms for multilayer J2-plasticity. *Computer methods in applied mechanics and engineering, 189(2). https://doi.org/10.1016/S0045-7825(99)00323-0.*

Montáns F.J. (2001) – Implicit multilayer J2-plasticity using Prager's translation rule. *International Journal for Numerical Methods in Engineering, 50(2). https://doi.org/10.1002/1097-0207(20010120)50:2<347::AID-NME28>3.0.CO;2-Q.*

Mroz Z. (1967) – On the description of anisotropic workhardening. *Journal of the Mechanics and Physics of Solids, 15(3). https://doi.org/10.1016/0022-5096(67)90030-0.*

Picart D. (1993) – Comportement et mise en forme d'un explosif agrégataire. *PhD thesis. https://www.theses.fr/1993DENS0007.*

Picart D., Benelfellah A., Brigolle J.L., Frachon A., Gratton M., Caliez M. (2014) – Characterization and modeling of the anisotropic damage of a high-explosive composition. *Engineering Fracture Mechanics, 131. https://doi.org/10.1016/j.engfracmech.2014.09.009.*

Picart D., Pompon C. (2016) – Experimental characterization of the multiaxial failure of a plastic-bonbed explosive. *International Journal of Energetic Material and Chemical Propulsion, 15(2). https://doi.org/10.1615/IntJEnergeticMaterialsChemProp.2016013662.*

Plassart G., Picart D., Gratton M., Frachon A., Caliez M. (2020a) – Quasistatic mechanical behaviour of HMX- and TATB-based plastic-bonded explosives. *Mechanics of Materials, 150. https://doi.org/10.1016/j.mechmat.2020.103561.*

Plassart G. (2020b) – Comportement mécanique anisotrope induit des explosifs comprimés. *PhD thesis. https://hal.archives-ouvertes.fr/tel-03199577.*

Rangaswamy P., Thompson D.G., Liu C., Lewis M.W. (2010) – Modelling the mechanical response of PBX 9501. *14th International Detonation Symposium. https://permalink.lanl.gov/object/tr?what=info:lanl-repo/lareport/LA-UR-10-01416.*

Rinaldi R.G. (2006) – Loi physique de comportement des polymères amorphes et intégration dans un code éléments finis. *PhD thesis. https://tel.archives-ouvertes.fr/tel-00103408.*

Tan H., Huang Y., Liu C., Ravichandran G., Inglis H.M., Geubelle P.H. (2007) – The uniaxial tensile of particulate composite materials with non-linear interface debonding. *International Journal of Solids and Structures, 44(6). https://doi.org/10.1016/j.ijsolstr.2006.09.004.*

Tan H., Liu C., Huang Y., Geubelle P.H. (2005) – The cohesive law for the particle/matrix interfaces in high explosives. *Journal of the Mechanics and Physics of Solids, 53(8). https://doi.org/10.1016/j.jmps.2005.01.009.*

Thompson D.G., Wright W.J. (2004) – Mechanical Properties from PBX 9501 pressing study. *AIP Conference Proceedings 706, 503, https://doi.org/10.1063/1.1780287*

Thompson D.G., Brown G.W., Olinger B., Mang J.T., Patterson B., DeLuca R., Hagelberg S. (2010) – The effects of TATB ratchet growth on PBX 9502. *Propellants, Explosives, Pyrotechnics, 35(6). https://doi.org/10.1002/prep.200900067.*

Trumel H., Rabette F., Willot F., Brenner R., Ongari E., Biessy M., Picart D. (2019) –**.** Understanding the thermomechanical behaviour of a TATB-based explosive via microstructure-level simulations. Part I: Microcracking and viscoelasticity. *Europyro 44th International Pyrotechnics Seminar. https://hal.archives-ouvertes.fr/hal-02312483.*

Van Mier J.G.M. (1984) – Strain-softening of concrete under multiaxial loading conditions. *PhD thesis. https://citeseerx.ist.psu.edu/viewdoc/download?doi=10.1.1.980.2406&rep=rep1&type=pdf.*

Van Mier J.G.M. (1986) – Multiaxial strain-softening of concrete. Part II: Load-Histories. *Materials and structures, 19*(3). *https://doi.org/10.1007/BF02472035*.

Wu Y.Q., Huang F.L. (2009) – A micromechanical model for predicting combined damage of particles and interface debonding in PBX explosives. *Mechanics of Materials, 41(1). https://doi.org/10.1016/j.mechmat.2008.07.005.*

Yan H., Oskay C. (2017) – Multi-yield surface modeling of viscoplastic materials. *International Journal for Multiscale Computational Engineering, 15(2). https://doi.org/10.1615/IntJMultCompEng.2017020087.*

Zubelewicz A., Thompson D.G., Ostoja-Starzewski M., Ionita A., Shunk D., Lewis M.W., Lawson J.C. Kale S., Koric S. (2013) – Fracture model for cemented aggregates. *AIP Advances, 3(1). https://doi.org/10.1063/1.4789791.*

1